LYRA – I. Simulating the multiphase ISM of a dwarf galaxy with variable energy supernovae from individual stars

Thales A. Gutcke [ID],⋆ Rüdiger Pakmor [ID], Thorsten Naab and Volker Springel [ID]

Max-Planck-Institut für Astrophysik, Karl-Schwarzschild-Straße 1, D-85748 Garching, Germany

ABSTRACT

We introduce the LYRA project, a new high-resolution galaxy formation model built within the framework of the cosmological hydrodynamical moving mesh code AREPO. The model resolves the multiphase interstellar medium (ISM) down to 10 K. It forms individual stars sampled from the initial mass function (IMF), and tracks their lifetimes and death pathways individually. Single supernova (SN) blast waves with variable energy are followed within the hydrodynamic calculation to interact with the surrounding ISM. In this paper, we present the methods and apply the model to a $10^{10}\,M_\odot$ isolated halo. We demonstrate that the majority of SNe are Sedov resolved at our fiducial gas mass resolution of $4\,M_\odot$. We show that our SN feedback prescription self-consistently produces a hot phase within the ISM that drives significant outflows, reduces the gas density, and suppresses star formation. Clustered SNe play a major role in enhancing the effectiveness of feedback, because the majority of explosions occur in low-density material. Accounting for variable SN energy allows the feedback to respond directly to stellar evolution. We show that the ISM is sensitive to the spatially distributed energy deposition. It strongly affects the outflow behaviour, reducing the mass loading by a factor of 2–3, thus allowing the galaxy to retain a higher fraction of mass and metals. LYRA makes it possible to use a comprehensive multiphysics ISM model directly in cosmological (zoom) simulations of dwarf and higher mass galaxies.

Key words: methods: numerical – stars: luminosity function, mass function – galaxies: formation – ISM: evolution – ISM: structure.

1 INTRODUCTION

In the current paradigm of galaxy formation in a Λ cold dark matter (ΛCDM) universe, the non-linear baryonic physics involved in structure formation and galaxy build-up is an active area of research. Not only may baryons play an important role in shaping dark matter halo profiles (e.g. El-Zant, Shlosman & Hoffman 2001; Weinberg & Katz 2002; Read & Gilmore 2005; Pontzen & Governato 2012), but also the details of the star formation (SF) process and the ensuing injection of energetic feedback from supernovae (SNe) are decisive to the formation and evolution of luminous galaxies (Larson 1974; White & Rees 1978; Saito 1979; Dekel & Silk 1986; Mac Low & Ferrara 1999). In the centres of dark matter haloes we expect gas to collapse into molecular clouds, cool radiatively, and fragment to form stars. Stars are expected to emit radiation and in some cases die as SNe, ejecting energy and enriching the interstellar medium (ISM) with metals. The metals, in turn, enhance the cooling process and the cycle repeats.

Cosmological, hydrodynamic simulations of galaxy formation have been instrumental in developing our present understanding of the baryon cycle in galaxies. However, modelling the relevant processes has proven to be non-trivial, leaving many uncertainties unresolved. Dwarf galaxies are particularly interesting laboratories to study galaxy formation. Interest in these systems truly began to surge after the Sloan Digital Sky Survey discovered a large population of ultrafaint and classical dwarfs in and around the Milky Way (e.g. Willman et al. 2005; Belokurov et al. 2006); see Simon (2019) for a review. Because they are simultaneously low mass and dark matter dominated, dwarf galaxies are a critical testing ground for dark matter models. Additionally, they are extreme environments in terms of mass, metallicity, and size. Their shallow potential wells make them highly sensitive to reionization and feedback, while making them also easier to model computationally than larger systems. Thus, the past decade has given rise to many published studies achieving substantial progress in our theoretical understanding of dwarf galaxies and their place in galaxy evolution (e.g. Governato et al. 2010, 2015; Sawala et al. 2011; Munshi et al. 2013; Simpson et al. 2013; Oñorbe et al. 2015; Trujillo-Gomez et al. 2015; Frings et al. 2017; Macciò et al. 2017).

The ISM in such cosmological simulations has often been modelled with effective (subgrid) models, for example following Springel & Hernquist (2003). This prevents the self-consistent formation of cold ($T < 10^4$ K) and dense ($n_H > 1$ cm^{-3}) gas, primarily for computational reasons. An ISM modelled in such a way does not form giant molecular clouds (GMCs), which are known to be the sites of SF. Without these structures, the local conditions into which stars form cannot be resolved. Moreover, this low-temperature ISM may be critical for resolving the effect of feedback especially in low-mass systems that are very sensitive to individual feedback events.

Recently, it has become computationally feasible to run high-resolution cosmological zoom-in simulations of field dwarfs with a resolved ISM that includes cooling below 10^4 K. For example, a simulation project that has made significant progress simulating

cosmological dwarf galaxies with a multiphase ISM is Smith, Sijacki & Shen (2019) using the model developed in Smith, Sijacki & Shen (2018). The authors present five dwarfs in the halo mass range 2.5–$6 \times 10^9 \, M_\odot$ that they run to $z = 4$ with a baryonic mass resolution of $\sim 300 \, M_\odot$. Using single stellar population (SSP) star particles and a SN feedback prescription that injects momentum instead of thermal energy when the SN is estimated to be underresolved, they conclude that other forms of stellar feedback beyond SNe alone are necessary to explain the low SF efficiencies observed in dwarf galaxies.

The Engineering Dwarfs at Galaxy formation's Edge (EDGE) project (Agertz et al. 2020) presented a $10^9 \, M_{\rm halo}$ dwarf galaxy resolving down to $\sim 300 \, M_\odot$ SSPs for which they resolve the multiphase ISM, individual SNe, and radiation via radiation transfer (with RAMSES-RT; Rosdahl et al. 2013) from young stars in a cosmological context. They conclude that the galaxy-averaged stellar metallicity is a sensitive indicator able to discriminate between feedback models. They also show that the radiation significantly affects the growth of the galaxy. Runs with radiation have lower stellar masses by about an order of magnitude. They attribute this to the radiative heating of much of the gas to $\sim 10^4$ K, preventing it from cooling and condensing to densities above their SF threshold.

The Feedback In Realistic Environments 2 (FIRE-2) galaxy formation model presented in Hopkins et al. (2018) introduced a method to help resolve SN blast waves by adding the unresolved momentum explicitly, while also accounting for low-temperature cooling. Using this model, Wheeler et al. (2019) simulate three high-resolution cosmological dwarf galaxies at a mass resolution of $\sim 30 \, M_\odot$ with $z = 0$ virial masses of ~ 2–$10 \times 10^9 \, M_\odot$, testing their survival throughout reionization. In most cases SF is quenched before $z = 10$ due to reionization. The more massive systems have residual SF until $z \sim 2$–4 that is kept going due to gas being self-shielded.

Concurrently, non-cosmological simulations of individual clouds and stratified discs have made great strides to develop more accurate models of the ISM and capture baryonic feedback effects on a much smaller scale (e.g. Glover & Mac Low 2007; Kim & Ostriker 2015, 2017; Walch & Naab 2015; Walch et al. 2015; Girichidis et al. 2016; Simpson et al. 2016; Hirai, Fujii & Saitoh 2020; Kannan et al. 2020a; Smith et al. 2020). A critical insight into the process of SN feedback that has emerged from these efforts is that the density into which a SN shock expands is crucial to its effect on the ISM and, thus, the galaxy as a whole (see Naab & Ostriker 2017, for a discussion). SNe in dense environments have a negligible effect both dynamically and thermally (e.g. see Gatto et al. 2015). The largest feedback effect (preventing SF) is caused by SNe expanding into lower density regions and heating a significant fraction (depending on the simulation, 50–90 per cent of the volume of the ISM) to $\sim 10^6$ K. According to Gatto et al. (2015), this is only achieved numerically if the SN is injected thermally. Momentum injection accounts for the unresolved dynamical contribution of the SNe but does not produce a hot phase that is essential for driving outflows and preventing SF (Hu 2019; Steinwandel et al. 2020). Additionally, SNe in dense gas are more difficult to resolve numerically, since their Sedov radii are small (~ 1 pc) and the onset of the momentum conserving phase occurs much more quickly than for SNe expanding into more diffuse gas. Fortunately for simulations, a large fraction of stars are born in star clusters (Lada & Lada 2003) that in turn leads to the SNe being clustered as well. Thus, the majority of SNe explode into the evacuated regions of previous SNe, making them easier to resolve numerically while at the same time enhancing their feedback impact.

Recently, these improved ISM and feedback models are being put to the test on isolated dwarf galaxy simulations using particle-based (Hu et al. 2016, 2017; Lahén et al. 2019, 2020) and Eulerian grid codes (Emerick, Bryan & Mac Low 2019, 2020). These models are able to begin disentangling the relative contribution of different feedback processes such as SNe, stellar winds, and radiation for young stars while comparing the results to integrated galaxy properties. Hu et al. (2017) considered feedback from individual massive stars and a chemical network allowing for the formation of a multiphase ISM with a resolved cold, warm, and – of particular importance – hot phase (see e.g. Steinwandel et al. 2020). This is also the basic model for the GRIFFIN project (Lahén et al. 2020) that studies a merger-driven dwarf galaxy starburst with individual massive stars at subparsec resolution, and investigates the self-consistent formation of star clusters. Smith (2020) also uses an isolated dwarf galaxy to test the effects of a sampled initial mass function (IMF) relative to using an integrated IMF prescription. Thus, there is a growing body of work showing that the details of the SF and feedback processes have a significant impact on the resulting galaxy properties.

In this work, we introduce LYRA, a novel galaxy formation physics model for the moving mesh code AREPO with low-temperature cooling and resolved feedback from individual stars. The aim of this new model is to attain sufficiently high mass resolution that individual blast waves are resolved, thereby eliminating many of the uncertainties associated with the subgrid modelling of SN energy injection. This, in turn, enables the model to capture the interaction of the SN blast waves with the ISM and the subsequent formation of outflows.

Simultaneously, we make modelling choices that allow the use of this model in cosmological zoom-in initial conditions of dwarf galaxies. This paper details the model and presents the first tests using an isolated low-mass dwarf galaxy. In Paper II (Gutcke et al., in preparation), we will analyse cosmological zoom-in simulations using the LYRA model.

This paper is organized as follows. Section 2 describes the implementation details of the LYRA model. Section 3 examines how well individual SNe are resolved, while Section 4 applies the LYRA model to an isolated dwarf galaxy and details its feedback properties. In Section 5, we compare our results to previous work and discuss limitations due to missing physics, while Sections 6 summarizes our conclusions. Appendix A presents convergence and parameter tests.

2 THE LYRA MODEL

2.1 Framework

Our model is built into the moving mesh magnetohydrodynamics (MHD) code AREPO (Springel 2010; Pakmor et al. 2016; Weinberger, Springel & Pakmor 2020). It solves the MHD equations on an unstructured Voronoi mesh that adapts itself to the gas flow using a second-order finite volume scheme. In this way AREPO combines the accuracy of Eulerian finite volume schemes, in particular their superb shock capturing abilities, with advantages offered by Lagrangian codes, such as their excellent spatial adaptivity and accuracy for high bulk flow velocities.

In the quasi-Lagrangian mode of AREPO, the mesh-generating points that are used to construct the Voronoi tessellation follow the gas motions, with a small correction to keep the mesh regular (Vogelsberger et al. 2013). Owing to the non-linear nature of the MHD equations, cells can still accumulate or lose mass over time. Therefore, to keep the mass of the cells within a factor of 2 of our target mass resolution, we employ explicit refinement and

derefinement operations. We split a cell into two cells when its mass surpasses twice the target mass resolution and merge it with its neighbours when its mass falls below half of the target mass resolution. In addition, we require that neighbouring cells do not differ by more than a factor of 10 in volume, otherwise we refine the larger cell. The quasi-Lagrangian approach is intrinsically adaptive to density, resolving higher density regions at better spatial resolution. Moreover, it guarantees that the spatial resolution does not change abruptly at steep density gradients.

Dark matter and stars are treated as collisionless particles and the total gravitational force for all resolution elements is computed using the hierarchical tree method (Barnes & Hut 1986; Springel 2005). The coupled system of MHD and gravity is then integrated using a second-order leapfrog scheme.

AREPO also includes a hierarchical local time stepping scheme that allows us to integrate every resolution element at the time step it requires. For a multiscale problem like galaxy formation this can save significant computational time compared to integrating all resolution elements at the minimum global time step required for any resolution element. However, it introduces additional challenges for the implementation of source terms as described in Section 2.5. In the following we describe the primary additional source terms that we have added to model the physical processes of radiative cooling, SF, and stellar feedback.

2.2 Heating and cooling

We model the external ultraviolet background (UVB) as a spatially uniform radiation field that provides a heating term and varies with time. We take its tabulated value from Faucher-Giguère (2020) and include it as a heating term in the hydrogen and helium cooling calculation. The UVB sets in at redshift $z \approx 9$ and rises until it peaks at $z \approx 6$–7. Atomic hydrogen and helium are self-shielded from the UVB following Rahmati et al. (2013), who fit the hydrogen shielding column to radiative transfer simulations. This results in a redshift- and density-dependent self-shielding factor that increases with increasing density from zero to unity. The heating of hydrogen and helium by the UVB is reduced by this factor for every cell at each active time step. As such, gas cells with densities above $n_H \approx 0.01 \text{ cm}^{-3}$ will have self-shielding factors of 1, and will not be heated by the UVB. In the idealized simulation we present in this work, we use the $z = 0$ values of the UVB. While heating in the form of photoionization and photoelectric heating are important physical processes in the ISM, we have not included these in the current model and discuss the implications of this in Section 5.

To model the gas cooling, we allow hydrogen and helium to exchange energy via two-body processes including collisional excitation, collisional ionization, recombination, dielectric recombination, and free–free emission. Additionally, there is inverse Compton cooling off the cosmic microwave background (CMB). These processes put together constitute primordial atomic cooling of hydrogen and helium. They allow gas to cool down to $\sim 10^4$ K, but become inefficient below this temperature. We implement them following the chemical network of Katz, Weinberg & Hernquist (1996), which is the same as in the Illustris simulation described in Vogelsberger et al. (2014). Once the primordial gas becomes chemically enriched through the metal ejection from SN explosions and asymptotic giant branch (AGB) mass return, these additional elements can contribute significantly to the cooling. However, following the injection and ionization states of each element individually is currently beyond the computational scope of our model. For each gas cell, we trace the abundance of the nine most common elements (H, He, C, N, O, Mg,

Si, Mn, and Fe) and use these to compute the total metallicity of the cell. Then, we assume collisional ionization equilibrium and tabulate the heating and cooling rates for processes not included in the Katz et al. (1996) network. We note that we use the solar abundances of Asplund et al. (2009) and assume $Z_\odot = 0.01337$ throughout this work.

Metal line cooling, low-temperature cooling, and molecular cooling (including H_2) are tabulated using the CLOUDY (v17.01; Ferland et al. 2017) equilibrium calculations by Ploeckinger & Schaye (2020). We use the publicly available version 'UVB_dust1_CR0_G0_shield1' that self-consistently models the attenuation by low-temperature gas of the UV radiation with a temperature- and density-dependent shielding column. This includes the use of CLOUDY's 'Orion' dust model. The input radiation field that Ploeckinger & Schaye (2020) used during the creation of CLOUDY is the same as the UVB we use. During the simulation, the cooling rate generated by the metal component of a cell is obtained by interpolating the table, which contains the dimensions of redshift, hydrogen number density, temperature, and metallicity. This is similar to Vogelsberger et al. (2014), but with the addition of a metallicity dimension to take the metallicity dependency of the cooling rates explicitly into account and an extended range to higher densities. Redshift is tabulated in the range $z = 9$–0, hydrogen number density between $\log(n_H/\text{cm}^{-3}) = -8$ and 6, temperature between $\log(T/K) = 1$ and 9, and metallicity between $\log(Z/Z_\odot) = -4$ and 0.5. Above the last metallicity bin, the cooling rate is determined by scaling the solar value with the metallicity value in solar units. Below our lowest metallicity we instead use the lowest tabulated value since the cooling rates below $\log(Z/Z_\odot) = -4$ are minimally different. The total cooling rate of a given cell is then computed as

$$\Lambda_{\text{cell}} = \Lambda_{\text{prim}} + \Lambda_{\text{metal}} + \Lambda_{\text{low temp}}. \tag{1}$$

To extract just the metal cooling contribution we subtract the primordial rates (which are calculated in the Katz et al. 1996 network) from the ones obtained including molecules and metals (see Wiersma, Schaye & Smith 2009, for a detailed investigation using this method). We note that our cooling does not take the relative abundances of different elements into account.

Our low-temperature cooling is comparable to the fitting formula from Hopkins et al. (2018), which was obtained by fitting to CLOUDY modelling including low-temperature metal line, fine structure, and molecular rates, also assuming collisional ionization equilibrium (this is also used in Marinacci et al. 2019).

2.3 Formation of single stars

Once gas cells are able to cool and contract we expect stars to form in the densest clumps. Star cluster forming clumps have an average density of 10^3–10^5 cm^{-3} (Lada & Lada 2003; Klessen 2011). Thus, we set the onset of SF to $n_H > 10^3$ cm^{-3}. A different choice for this parameter does not strongly impact our results (as shown in Appendix A). We set the efficiency parameter to 0.02. The star formation rate (SFR) $\dot{M}_{\star,i}$ of a cell i is calculated according to the Schmidt relation

$$\dot{M}_{\star,i} = \epsilon_{\text{SF}} \frac{M_i}{t_{\text{ff}}}, \tag{2}$$

where ϵ_{SF} is the star formation (SF) efficiency and M_i is the mass of the cell. The free-fall time of a cell is $t_{\text{ff}} = \sqrt{3\pi/(32\,G\rho_i)}$. To have a non-zero SFR, we additionally require the temperature of the gas cell to be $T < 100$ K.

SF itself is implemented stochastically, i.e. the SFR of a cell translates to a probability of creating a star particle in a given time
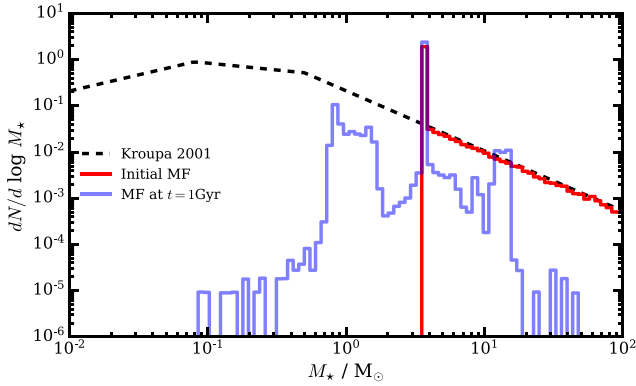
Figure 1. Initial stellar mass function and current stellar mass function at later times, as labelled. The IMF below $4\,M_\odot$ is *unresolved*, i.e. it is not individually sampled. However, the integrated mass from the unresolved part is distributed into $4\,M_\odot$ stars that create the visible spike at this mass scale. These *unresolved* stars do not lose mass or age, thus this spike also remains at later times.

step. Each cell can only form a single star per time step. The mass of the potentially created star, $M_{\star,\,\mathrm{new}}$, is drawn from the (mass-weighted) IMF. The probability $\mathcal{P}$ for a cell i to create a star during a time step $\mathrm{d}t$ is given by

$$\mathcal{P}_i = \frac{M_i}{M_{\star,\,\mathrm{new}}} \left[1 - \exp\left(-\epsilon_{\mathrm{SF}} \frac{\mathrm{d}t}{t_{\mathrm{ff}}} \right) \right]. \tag{3}$$

As can be seen in the red line in Fig. 1, we truncate our IMF to $M_{\star,\,\mathrm{min}}$, which is set to $4\,M_\odot$ in this paper. Effectively, we thus follow two types of star particles. *Resolved* stars populate the properly sampled part of the IMF and have masses above $M_{\star,\,\mathrm{min}}$. These stars follow the stellar evolution pathways described in Section 2.4, meaning they may return mass, metals, and energy depending on their initial mass. *Unresolved* star particles all have masses of exactly $M_{\star,\,\mathrm{min}}$. These star particles do not return mass, metals, or energy to the ISM. They merely sample the low-mass end of the IMF and provide a gravitational/dynamical contribution. To not overestimate the stellar mass that is to be formed according to the SFR, we guarantee that the total mass of unresolved star particles equals the integrated mass in the IMF that would otherwise be present between $0.01\,M_\odot$ (the lower end of the IMF) and $M_{\star,\,\mathrm{min}}$.

Our prescription creates a tail of high-density cells whose radii can become much smaller than our gravitational softening length of the gas. Moreover, we do not include the relevant physical processes that dominate at these densities. Thus, we set $\mathcal{P} = 1$ for all cells with $n_{\mathrm{H}} > 10^4\,\mathrm{cm}^{-3}$. This enforced SF is similar to the treatment by Lahén et al. (2020). As our tests in Fig. A1 show, this choice has a negligible effect on the SFR (see Smith et al. 2019, for a detailed analysis of the effects of increased SF efficiency).

In highly resolved simulations where smoothed particle hydrodynamics (SPH) particles or hydrodynamical cells become less massive than individual stars, the question arises where to draw mass from to actually form new stars. A common solution to this issue is to create sink particles that accrete mass for a time until they take on the characteristics of star particles (e.g. Krumholz, McKee & Klein 2004; Federrath et al. 2010; Walch et al. 2015). This method requires mass to be decoupled from the hydrodynamic calculation while the sink particle 'grows' until it can make a massive star. Another solution is to accumulate sufficient star forming material before spawning a massive star. This technique was used in Hu et al. (2017), but requires instantaneous transfer of mass over the whole

galaxy when not enough star-forming gas is available locally. This can be avoided by defining a spatially located accretion region (see Hu 2019; Hirai et al. 2020).

We opt to create stars instantaneously by defining an accretion radius for the 'star-forming region' around a star-forming cell (similar to the method in the SImulations Resolving IndividUal Stars (SIRIUS) project presented in Hirai et al. 2020). The initial guess of the accretion radius is set to encompass all cells that share an interface with the star-forming cell. There are on average $\sim$20 of such nearest neighbours. If the mass enclosed within this radius is not at least twice the mass of the star to be formed, the radius is increased until this criterion is met. Once the radius is found, the star is formed by drawing an equal fraction f_{acc} of mass from each cell within the accretion radius. This way, the mass of each cell within the radius is reduced at most by half, and no cells are fully evacuated due to the formation of the star particle. The new star inherits the centre-of-mass, total momentum, and metal content of the gas that has been removed from cells to form it, which guarantees conservation of mass and metal mass, as well as momentum. The stellar metallicity is then calculated as the ratio of the metal mass and the star's mass.

Before creating the stars in a given time step, the model checks whether any cell is within the accretion region of two or more stars. If this is the case, and if there is not enough mass within the cell to provide the requested mass to each to-be-formed star, formation of the least massive star is cancelled. If needed, this cancellation is repeated until the mass budget is positive. We point out that this a fix for extremely rare circumstances. For example, in our fiducial run this occurred a single time in the 1 Gyr run time.

2.4 Individual supernovae with variable energy

As each massive star particle is an individual star, it can produce at most one SN within its lifetime. We note that for now we do not take binary stars into consideration. However, in future work we plan to add a prescription for a non-zero binary fraction and account for their modified evolution. Thus, each stellar death induces a discrete explosion event. We ensure that the corresponding blast wave is time resolved by reducing the local simulation time step accordingly (see Section 2.5).

We use the SN explosion models of Sukhbold et al. (2016) to infer the energy of the SN (varying from 0 to 1.8×10^{51} erg) from the initial mass of each star. These models are able to predict a fluctuating energy since they follow the non-monotonic variation in core compactness prior to explosion. They are based on one-dimensional calculations that follow $\sim$2000 nuclei, assume solar abundance SN progenitor stars, and include neutrino transport. When a star reaches the end of its lifetime, we inject the energy, mass, and metals according to Fig. 2 into the single cell that hosts the star in that particular time step.

We choose $M_{\mathrm{SN,min}} = 8\,M_\odot$ as our SN threshold mass. However, according to Sukhbold et al. (2016), there are some progenitor masses that do not produce SNe despite being above $8\,M_\odot$. These stars are assumed to directly collapse to form black holes instead. Thus, by following this model, we indirectly take this mode of stellar mass black hole formation into account. The corresponding stars nevertheless eject mass and metals into the ISM. However, we note that our metallicities may be overestimated due to the use of solar abundance SN models (see Section 5).

As our model does not yet include a stellar wind prescription, we inject both the wind and SN (mass and metal) returns simultaneously. Additionally, we choose to inject a minimum of 10^{49} erg per star above $8\,M_\odot$ at its death to account for some of the (otherwise
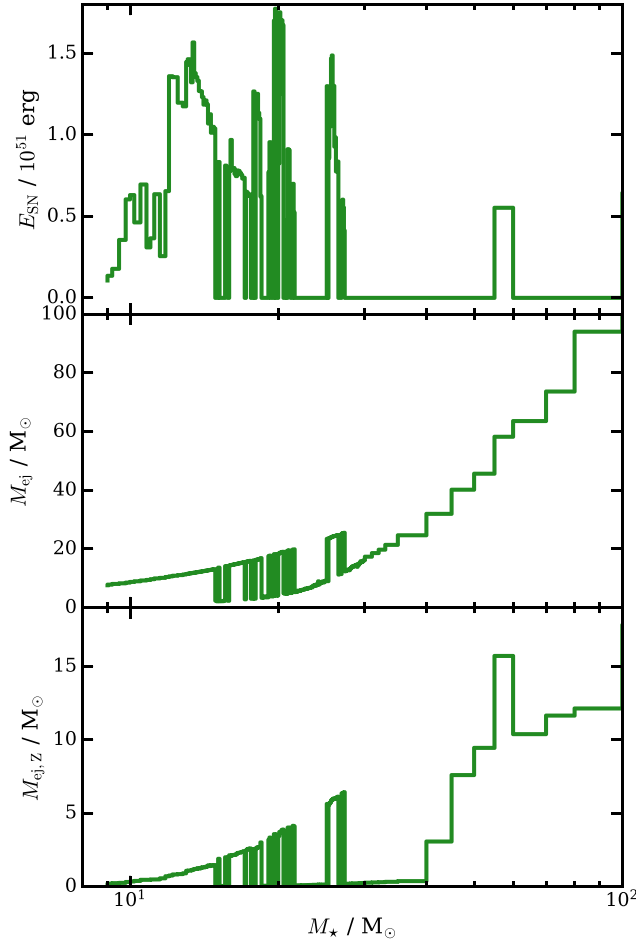
Figure 2. Energy, total mass, and mass in metals ejected per supernova (SN) as a function of initial stellar mass, from top to bottom. These values include the SN and wind ejecta presented in Sukhbold et al. (2016), and are tabulated and interpolated during run time of the simulation.

neglected) wind energy. The mean energy injected per star with mass above $M_{SN, min}$ is 4.4×10^{50} erg (see Table 2). This means that our model injects a factor of ~2 less energy than a model that simply accounts for 10^{51} erg per massive star. The lifetimes of stars above our SN threshold are taken from Portinari, Chiosi & Bressan (1998) and are metallicity dependent. To test whether our SNe are Sedov resolved at our fiducial resolution, we run separate tests in isolated boxes and check that a sufficient fraction of the thermal energy we inject is converted into kinetic energy within the hydrodynamic calculation (see Section 3).

2.5 Time steps to resolve supernovae

We integrate the system using individual, variable time stepping in a power-of-two hierarchy according to Springel (2010). The initial estimate of the hydrodynamical time step t_i necessary for a cell i is determined from the Courant criterion (Courant, Friedrichs & Lewy 1967) according to

$$\Delta t_i = C_{CFL} \frac{R_i}{c_i + |v_i|}, \tag{4}$$

where $C_{CFL} = 0.3$ is the Courant factor, $R_i = (3V_i/4\pi)^{1/3}$ the spherical radius of the cell, $c_i = \sqrt{\gamma P_i/\rho_i}$ the sound speed of the cell, and v_i the velocity of the cell relative to the grid. This criterion captures

any physical changes happening to the cell itself. Additionally, there are a variety of non-local physical processes that may affect the cell. To resolve these, the cell's time step may need to be reduced below this initial value. We outline the most important ones here. First, the maximum time step cell i can have while still being aware of the (potentially supersonic) signals from other cells can be estimated from the signal velocity v_{sig} of cells in the vicinity (cf. Springel 2010):

$$v_{sig} = c_i + c_j - \boldsymbol{v}_{ij} \frac{\boldsymbol{r}_{ij}}{r_{ij}}, \tag{5}$$

where $\boldsymbol{v}_{ij}$ is the velocity difference between two cells i and j. The time that it can minimally take for a signal from cell j to cell i is then approximated as $\Delta t_{vicinity} = \frac{r_{ij}}{v_{sig}}$. Thus, the time step of cell i is set to $\min(\Delta t_i, \Delta t_{vicinity})$.

However, this criterion can only be aware of signal speeds already present within cells. In the case of a SN explosion, the energy is injected instantaneously at a given time independent of the depth of the time step hierarchy. Consequently, if a SN is injected into a cell that is on a lower time step than its neighbours, it is possible for the supersonic shock to pass the inactive cells before they are able to react due to their longer time steps. This behaviour can be highly insufficient to resolve the Sedov phase of the SN shock (see Durier & Dalla Vecchia 2012, for a detailed analysis).

Fortunately, the timing of the onset of a given SN explosion is predetermined by the initial mass of its stellar progenitor. Therefore, we can pass the information of an imminent SN to the time stepping routines *before* the SN is injected. Consequently, the cells are granted a lead time to adjust their time steps suitably. This is accomplished by tracking all stars that will explode within the next global time step. For a cell i that hosts one such star, the sound speed that it would have if the SN were injected is calculated according to

$$c_{SN} = \sqrt{\gamma(\gamma - 1)\left(u_i + \frac{E_{SN}}{M_i}\right)}, \tag{6}$$

where γ is the adiabatic index, u_i is the internal energy per unit mass, M_i the mass of the cell, and E_{SN} is the energy of the SN (which can vary, see Section 2.4). To obtain the desired result of making sure the cells in the vicinity of an imminent SN have low enough time steps to guarantee a time-resolved blast wave, it would be sufficient to set c_{SN} in equation (5) starting at the last global time step (defined as a time step where all cells are active) prior to injection. This, however, slows down the calculation considerably and partly unnecessarily. The time step hierarchy in our isolated runs is usually 5–6 levels deep, meaning that the smallest time step can be $2^6 = 64$ times smaller than the global time step. So, if for example the SN event happens towards the end of a global time step, the region around the 'to-be' SN will likely be needlessly on the lowest time step for the majority of the time.

Instead, we can steadily shorten the time steps toward the required time step $\Delta t_{SN} = R_i/c_{SN}$. Hence, we calculate a time step Δt_{max} for each SN host cell:

$$\Delta t_{max} = f_{SN}(t_{SN} - t_{now}), \tag{7}$$

where t_{SN} is the time of the supernova (SN), t_{now} is the time of the simulation, and $f_{SN} = 0.9$ is an ad hoc factor, the choice of which does not affect the results presented here. This requires that the cell will be active at least one more time before the SN event. This calculation is repeated again at the next active time. Thus, the time step is iteratively reduced until $c_{SN} > R_i/\Delta t_{max}$. This ensures that the cells surrounding the imminent SN will reduce their time steps

according to equation (5). When the SN is finally injected, the cells within reach of the signal speed of the shock will be prepared.

We note that the star can move from one host cell to another before the SN is injected. In this case, the new cell's time step is reduced instead. We do not expect this to affect the outcome, since the new cell is likely a neighbour of the former host. As such, its time step has already been reduced to a similar degree.

2.6 AGB mass return

At present the only form of non-SN stellar feedback in our model is the mass and metal return from asymptotic giant branch (AGB) stars (although we do account for some stellar wind energy, see Section 2.4). For AGB stars, we tabulate the mass return for each element as a function of initial stellar mass and stellar metallicity, following the models of Karakas et al. (2018). For simplicity, the mass return is injected all at once at the end of life of the star. The lifetimes of AGB stars are also determined from Karakas et al. and are initial mass and metallicity dependent. The mass of the star particle is reduced by this amount and the mass of the host gas cell is increased. Additionally, the mass for each element is increased by the metal mass created. The hydrodynamic distribution of the mass is then handled by AREPO's cell refinement.

3 TESTS FOR INDIVIDUAL SUPERNOVAE

A problem often faced by cosmological galaxy formation simulations that include SN feedback is that at the typical spatial and temporal resolution that can be afforded the thermal energy injected by SNe is quickly radiated away in cooling before hydrodynamics can transform a fraction of this energy into momentum. When this happens, feedback is numerically inefficient at heating and removing dense gas and preventing it from forming stars. In the literature, there are a variety of prescriptions to ameliorate this issue, i.e. injecting the energy as momentum (e.g. Navarro & White 1993; Springel & Hernquist 2003; Dalla Vecchia & Schaye 2008), preventing gas from cooling for a time after the SN is injected (e.g. Stinson et al. 2006), storing up energy until there is enough for the desired effect (Schaye et al. 2015), or adding additional momentum based on an estimate of how much energy will be numerically lost (Hopkins et al. 2018). Naab & Ostriker (2017) provide an excellent review of the various prescriptions and their merits.

Instead of following any one of these solutions, we set the mass resolution high enough to self-consistently produce most of the momentum from a thermally injected SN. The theoretical 'similarity solution' for a blast wave predicts an early energy conserving phase known as the Sedov–Taylor phase during which the total energy remains constant while the shock front moves outward. This phase ends when radiative cooling in the dense shell formed by the shock becomes dominant and energy is no longer conserved. At this time, the total energy is predicted to be distributed in thermal and kinetic energy following the ratio 72:28 (Chevalier 1976; Ostriker & McKee 1988). If indeed 28 per cent of the initial energy is converted to kinetic energy numerically, the SN is fully Sedov resolved.

We test to what extent the SNe in our simulation are Sedov resolved (Sedov 1959) by simulating individual SN explosions in isolated, uniform-density boxes at the fiducial resolution of our main simulations ($4\,M_\odot$ target gas mass). This is similar to the work by Kim & Ostriker (2015), Hu et al. (2016), Haid et al. (2016), and Steinwandel et al. (2020). To this end, we set up a grid of initial conditions with varying values of ambient density, ambient metallicity, and stellar progenitor mass. The bins are $\log(n_H/\mathrm{cm}^{-3})$

Table 1. Progenitor mass, supernova (SN) energy, mass return (from winds and SN), and metal mass return for the three SN tests shown in Fig. 3.

$M_{\mathrm{init}}/M_\odot$	$E_{\mathrm{SN}}/10^{51}\,\mathrm{erg}$	$M_{\mathrm{ej}}/M_\odot$	$M_{\mathrm{ej},Z}/M_\odot$
10	0.6041	8.54	0.31
20.5	1.6714	19.03	3.81
59.5	0.4972	56.97	4.87

$= -3$–4 in steps of 1, $\log(Z/Z_\odot) = \{-2, -1, 0\}$. The stellar masses are tested for three values of 10, 20, and $60\,M_\odot$. The progenitor mass then sets the SN energy with matching amounts of mass and metal ejecta, see Table 1. We set the ambient thermal energy of the gas following the equilibrium curve in our phase diagrams.

For each SN test box, we follow the total energy within the remnant, and how much kinetic energy is induced by the blast wave. Fig. 3 shows the maximum kinetic energy relative to the kinetic energy predicted by the analytic solution. This is 28 per cent of the energy of the SN. We show this energy ratio as a function of ambient density.

As can be seen in Fig. 3, the numerical results move towards the analytical solution for decreasing ambient densities. Since there is less mass to sweep up, the blast wave reaches the shell formation time later (see equation 7 in Kim & Ostriker 2015), and the shell is physically larger, giving the code time to resolve the processes better. As we will see in Fig. 13, the majority of our SNe explode in low-density regions. Thus, we judge > 90 per cent of the SNe to be well resolved. Interestingly, high initial energies are also better resolved. This can be explained by the higher energy contrast between the initial injection energy and the background temperature. There is almost no dependence on metallicity, although lower metallicities give marginally more accurate results due to the cooling rates being lower. We have also tested the hot gas fractions produced by our SNe and compared these to theoretical expectations. They are well matched within a factor of 2.

We note that tests with a multicell injection scheme yield a lower amount of kinetic energy than what is shown in Fig. 3. By injecting the energy into multiple cells, we increase the initial radius. In the case of high densities, the radius thus approaches the Sedov radius itself. This in turn renders the blast wave less well resolved.

4 RESULTS FOR AN ISOLATED DWARF GALAXY

To validate our new model, we present results from an idealized dwarf galaxy. For easy comparison, we choose identical initial conditions to the ones used in Hu et al. (2017, hereafter H17) and run the simulation at a mass resolution of $4\,M_\odot$. The initial conditions consist of a live dark matter halo with a Hernquist profile. The total halo mass is $M_{\mathrm{halo}} \approx 2 \times 10^{10}\,M_\odot$. Background stars and gas are placed within the halo following an exponential profile with a scale length of 0.73 kpc. The mass of the stellar disc is $2 \times 10^7\,M_\odot$, and that of the gas disc $4 \times 10^7\,M_\odot$. The scale height of the stellar disc is 0.35 kpc. Initially, there is no gas beyond the disc. The initial set-up was run for 200 Myr including SN explosions to create quasi-stationary turbulence within the gas. This was done by H17 to create more realistic initial structures and add pressure support to prevent early collapse. As we will see, these initial conditions do not produce the same effect in our model. We note that all following analysis includes only stars that form during the actual run time of our simulation, not the ones from the initial 200 Myr equilibration period or the initial conditions. Differently than H17, we choose to give the gas an initial
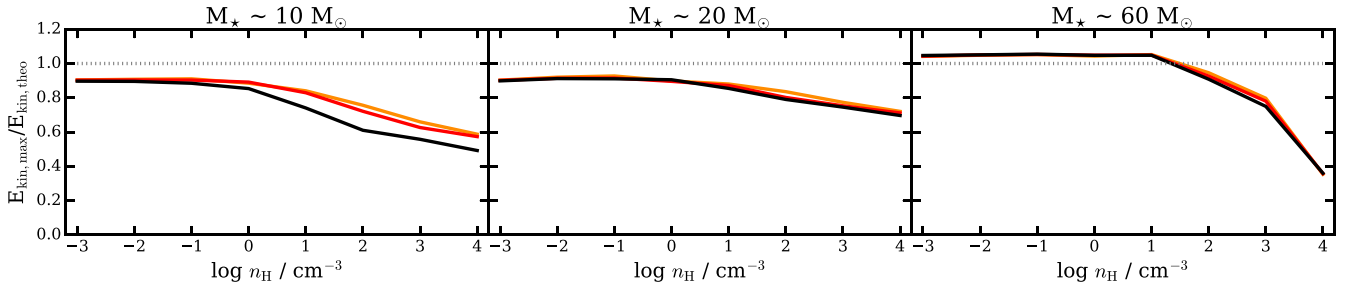
Figure 3. Kinetic energy at shell formation time normalized by the expected kinetic energy based on the analytic explosion solution, as a function of the ambient, homogeneous density of the surrounding medium. The panels show the results for a 10, 20.5, and 59.5 $M_\odot$ star, respectively. The three colours give in each case the results for different metallicities of the ambient medium. All the explosions include energy, mass, and metal injection according to our model values shown in Fig. 2. SNe in lower density environments are kinematically more resolved. At almost all tested densities, we reach the expected kinetic energy within a factor of 2.

metallicity of 0.01 $Z/Z_\odot$ (instead of 0.1). The value expected from observations of Local Group dwarfs (e.g. Kirby et al. 2013) at this stellar mass is 2–3 per cent. To transform the SPH initial conditions into ones usable for AREPO, we add a background grid of gas cells within a cubic box with a box size of 12 Mpc. During run time, AREPO refines and derefines cells as needed to adhere to our mass refinement criterion (see Springel 2010). Within $R_{\mathrm{crit, 200}}$ there are approximately 7.4 million gas cells and 2.8 million dark matter particles.

### 4.1 Model variations

We compare three versions of our model.

(i) VARIABLE_SN_ENERGY. The fiducial set-up as described in Section 2.

(ii) FIXED_SN_ENERGY. For this run we allow every star with initial mass above $M_{\mathrm{SN, min}}$ to be a SN with 10^{51} erg. The mass and metal return remains as shown in Fig. 2. Cumulatively, this model returns a factor of ~2.2 more energy per stellar mass than VARIABLE_SN_ENERGY (see Table 2). To a large degree, this is due to approximately 25 per cent of the high-mass stars in VARIABLE_SN_ENERGY not forming SNe but collapsing directly to black holes while ejecting mass and metals. This model is most closely comparable to the common assumptions made in cosmological simulations that sample stars via SSP particles and integrate the IMF to compute the returned SN energy.

(iii) NO_FB. In this simulation, we switch off all mass, metal, and energy returns from core-collapse SNe. Any metallicity increase in this run is due to AGB star returns alone.

4.2 Star formation history and the Kennicutt–Schmidt relation

We begin by analysing the star formation history (SFH; Fig. 4) of these three models. Since this is an idealized set-up, the SFR is highly dependent on the density distribution in the initial conditions. The SFR shows a strong increase that is similar across all runs during
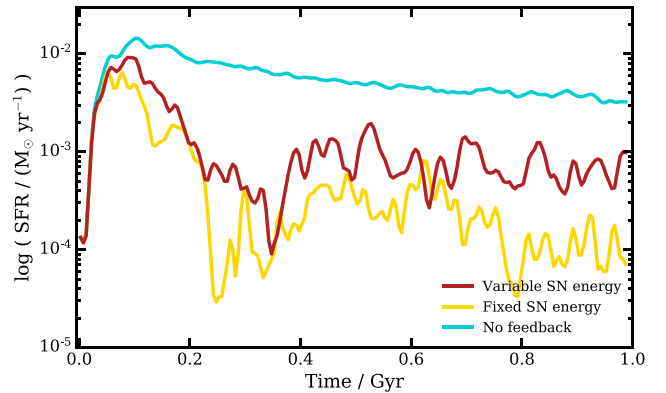

Figure 4. Star formation histories (SFHs) of our various isolated simulation runs. Models with feedback begin reducing their star formation rate (SFR) after the first burst, and retain a small SFR of ~10^{-3} $M_\odot$ yr^{-1} after 1 Gyr. Models without feedback yield a much higher SFR of ~10^2 $M_\odot$ yr^{-1} for the majority of the simulation time.

the first 80–100 Myr. After this initial time, we see the effects of the differing models. VARIABLE_SN_ENERGY increases until the energetic feedback from SNe begins to heat and blow out gas, decreasing the SFR. After about 400 Myr a bursty but overall steady SFR emerges at around 10^{-3} $M_\odot$ yr^{-1}. This is also the case for the FIXED_SN_ENERGY run, albeit the process begins earlier (so the peak is not as high) and the steady value is lower, since there is almost twice the amount of energy per SN (see Table 2). To investigate the driver of these differences, in Fig. 5 we show the mass and metal escape fractions beyond the virial radius. It is clear that FIXED_SN_ENERGY loses a much larger fraction of its gas mass and metals. Two-thirds of the produced metals end up beyond the virial radius and do not contribute to cooling and SF. This lack is the main driver of the lower SFR in this model. The SFR of NO_FB does not begin decreasing until a few Myr after VARIABLE_SN_ENERGY. When it does, the curve flattens out and then begins to drop slowly due to the lack of fuel for new stars.

Table 2. Total injected energy, mean energy injected per SN, mean energy injected per massive star (> 8 $M_\odot$), mean energy injected per total stellar mass, and number of SNe within the 1 Gyr run time of the simulation.

| Name	E_{inj} (10^{54} erg)	$E_{\mathrm{inj}}/N_{\mathrm{SN}}$ (10^{51} erg)	$E_{\mathrm{inj}}/N_\star(> 8\,M_\odot)$ (10^{51} erg)	$E_{\mathrm{inj}}/M_\star$ (10^{49} erg/$M_\odot$)	N_{SN} (10^3)
VARIABLE_SN_ENERGY	6.75	0.57	0.44	0.46	11.7
FIXED_SN_ENERGY	7.82	1.0	1.0	1.03	7.8
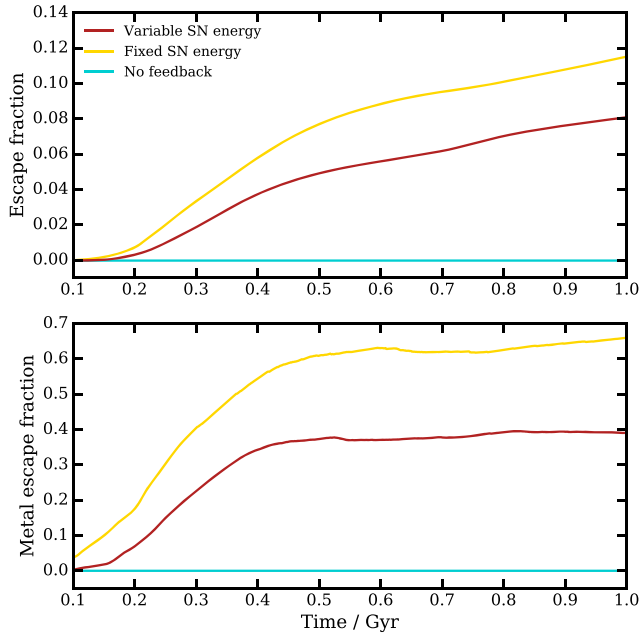
Figure 5. Fraction of gas that escapes the virial radius over time (upper panel) and fraction of metals produced that escape (lower panel) in our various isolated runs with SNe. Runs without SNe have zero escaped material. VARIABLE_SN_ENERGY loses less mass and less metals than the fixed energy models.

We investigate whether the SF may be triggered by the SNe that send shocks through the surrounding disc, compressing the gas. The top panel of Fig. 6 shows a face-on projection of the disc where the newly formed stars (formed within the last 1 Myr) are represented as red circles. They primarily sit on or near where the density gradient (in grey) is strongest. The lower panel shows a zoomed in representation of the area within the black square. Here, the colour map shows the pressure, while the peaks in the density gradient are indicated by black contours. Recent SF is now shown as white circles, while recent SN sites are indicated by white star symbols. It seems evident that the SNe carve out pressurized bubbles that expand. Where these bubbles run into material, they compress the gas, seen as the higher pressure at the edges of the bubbles. This is where new stars begin forming after the SN occurs. We even see a SN within the star-forming sites that is a short-lived, massive star that has already exploded.

Relating the available cold gas to the mass in stars formed in these models and comparing this to the observed Kennicutt–Schmidt relation is an informative way to understand whether our SF prescription performs well. Fig. 7 shows our models relative to observed galaxies. Since our initial conditions represent a dwarf galaxy, it is not surprising that our points end up at the very lower end of the Kennicutt–Schmidt relation. So much so that any comparison is uncertain, since this region of the relation is not well constrained. In general, it is however encouraging to see that all models with feedback lie close the extrapolation (solid and dashed lines) of the relation. In contrast, NO_FB clearly has a too high SF for the available gas density. VARIABLE_SN_ENERGY exhibits a SFR consistently above the lines. This is not surprising, since our model at present does not include any other form of energetic feedback except for core collapse SNe. Previous simulations have shown that the inclusion of radiative processes, magnetic fields, or stellar winds all work in the direction of reducing the SFR (e.g. Gatto et al. 2017; Peters et al. 2017; Girichidis
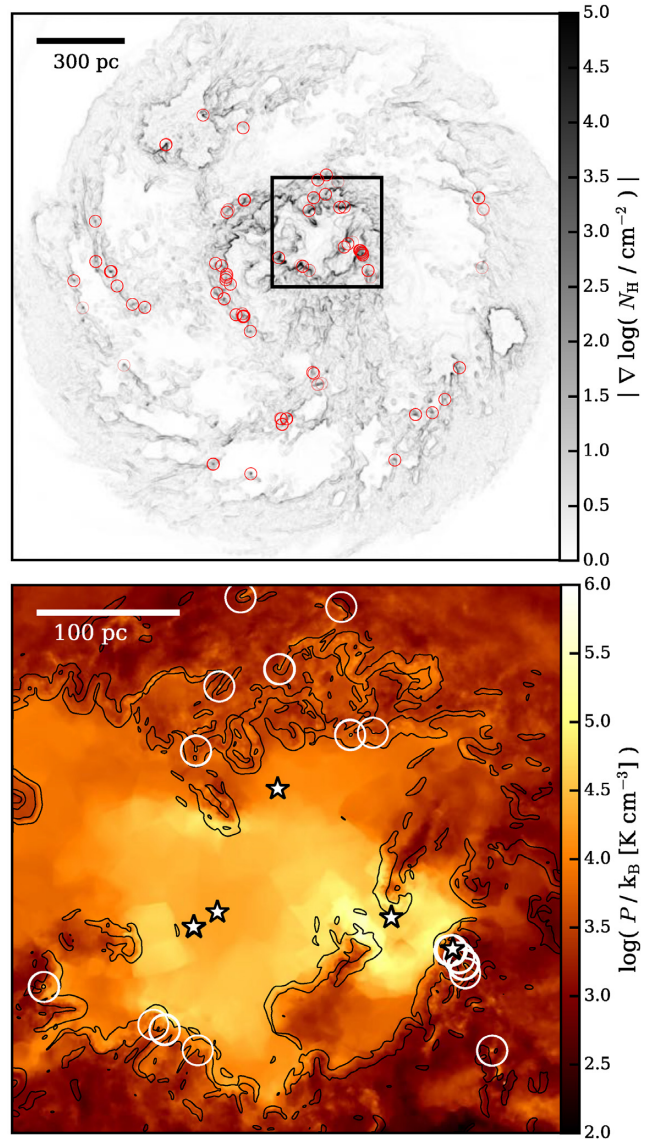

Figure 6. Upper panel: column density gradient in grey scale. Red circles indicate new SF sites within the last 1 Myr. The black square indicates the position of the zoom-in the panel below. Lower panel: The the colour map shows the pressure, while the black contours indicate the peak density gradient. White circles are sites of new SF within the last 1 Myr. White star symbols indicate locations of SNe between in the range $1 < t_{SN}/\mathrm{Myr} < 1.2$. The displayed simulation time is $t = 50\,\mathrm{Myr}$.

et al. 2018b). Interestingly, the SFR of FIXED_SN_ENERGY may be slightly lower than expectations, showing that this feedback prescription may be too strong. This model expels a larger fraction of the gas and metals (see Fig. 5). Note also that a truly fair comparison to observations requires detailed mocking that we postpone to a later paper.

4.3 Projections and phase diagrams

To gain a qualitative understanding of the differences between these models, we show face-on projections (projecting down the z-axis, assuming the disc lies in the x–y plane) of the gas in Fig. 8. The top row shows the hydrogen number density in a $6 \times 6 \times 3$ kpc box. The central row shows the mean temperature along the line of sight (z-axis), and the bottom row shows the mean metallicity.
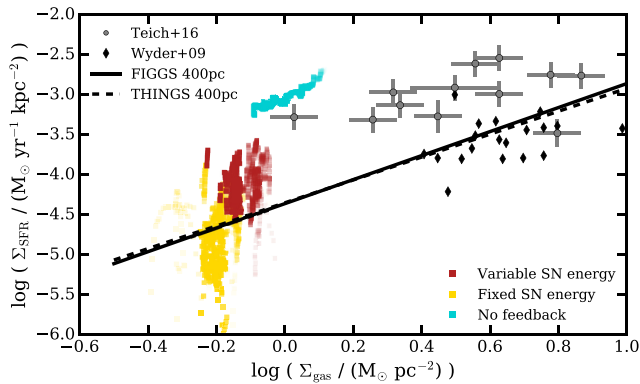
Figure 7. Kennicutt–Schmidt relation of our various isolated runs. Squares symbols are coloured according to the run, with low α values (high transparency) showing earlier times. Each data point is averaged over 10 Myr and over a cylindrical disc with a radius set by the maximum radius of stars at that time, and having a height of 200 pc. The grey error bars give the observed low-mass galaxies from the SHIELD sample (Teich et al. 2016). Black diamonds show the observations presented in Wyder et al. (2009). The solid black line represents the best fit from the FIGGS sample of dwarf irregular galaxies (Roychowdhury et al. 2014), while the dashed line is the best fit from the THINGS sample (Walter et al. 2008).

VARIABLE_SN_ENERGY has more cold and dense cloud structure in the inner 1 kpc radius and a higher metallicity in this area. Because of the stronger feedback in FIXED_SN_ENERGY, the region affected by the SNe is less dense and lacking in cold clouds. The metallicity is much lower in the central regions. In Fig. 9, we see the same but projected down the *y*-axis showing the edge-on view of the disc. Especially in the temperature projection it becomes apparent that the fixed energy model exhibits wider chimneys that expel more hot gas. The stronger outflows also significantly reduce the metallicity, not only in the disc but even beyond. The model that is most visibly different is NO_FB that exhibits no low-density or high-temperature gas. NO_FB also has almost no metallicity above the background metallicity of $10^{-2} Z_\odot$. The small enhancement is due to the AGB metal returns that is almost irrelevant on time-scales of the runtime of our simulations.

Another useful diagnostic is the phase diagram of gas. This is the two-dimensional distribution in the density–temperature plane. We show the mass (top row) and metallicity-weighted (bottom row) phase diagrams for all three models in Fig. 10. The dashed line in each panel shows $T = 10^4$ K, which is a common temperature cut-off in cosmological simulations and represents the approximate threshold between atomic and molecular cooling processes. The upper left-hand quadrant contains hot and low-density gas that is heated by SNe and then expands to lower densities. Since the SNe inject large amounts of metals, the metallicity in this gas phase is extremely high until it is mixed with the surrounding medium. Clearly, NO_FB does not exhibit any gas in this region. Without SNe, the gas follows the equilibrium curve. Cells in the lower left-hand quadrant are cold and diffuse. These are cells beyond the virial radius that have expanded adiabatically into the background volume of the simulation. Gas cells populating the lower right-hand quadrant are cool and dense. These cells follow the equilibrium cooling curve to lower temperatures and higher densities. The 'width' of the phase structure at temperatures $T = 10^2$–10^4 K and densities between $n_H = 10^{-2}$ and 10^2 cm^{-3} is due to the metallicity-dependent cooling. Higher metallicity gas cools at a faster rate, thus dropping its temperature while the density is still

relatively low. In other words, high-metallicity gas cools first and then condenses, while low-metallicity gas condenses and then cools.

This behaviour is best visible in NO_FB because there are no SNe to mix the metals. Here we see a strong metallicity gradient in the $< 10^4$ K gas. In the FIXED_SN_ENERGY model, the cold and dense gas is less metal rich. This is due to the stronger outflows caused by the enhanced SN energy that ejects a larger fraction of the metals (see Fig. 5). Another aspect to note is the metallicity distribution in the $> 10^4$ K gas in the runs with feedback. Here, the gas transitions from being metal enriched (pink) to having lower metallicity (green) while it cools from 10^8 down to 10^5 K. This gives an indication of the strength of metal mixing. FIXED_SN_ENERGY mixes more strongly.

4.4 Metallicity

The metals produced during the simulation are critical to the behaviour of the resulting galaxy. The gas cooling rates are strongly dependent on the metallicity, making enriched gas ($Z/Z_\odot \sim 1$) cool at a rate an order of magnitude higher than less enriched gas ($Z/Z_\odot \sim 0.1$) at the same density. Stars forming from dense cores inherit the metallicity of their cloud. A star's birth metallicity (with its birth mass) determines the star's lifetime. The higher the metallicity of a SN progenitor star, the shorter its life. In the case of AGB progenitor stars (in our model these are all stars with initial masses below 8 $M_\odot$, but without the stars in the unresolved part of the IMF) this trend is reversed. However the AGB metal returns are increased for higher metallicity stars. Thus, overall metal production is a runaway process where more metal-rich stars produce more metals in a shorter amount of time.

Fig. 11 shows the metallicity distribution function of all the gas cells within the simulation volume. Since we begin to evolve these idealized initial conditions at a metallicity of 1 per cent solar, there are no cells with a metallicity lower than this value. With no AGB returns and no SN returns, the distribution would remain a Dirac delta function at 1 per cent solar. So all higher metallicities in NO_FB (blue line) are due to AGB returns. We note that this is a logarithmic plot, so that the small differences visible between VARIABLE_SN_ENERGY (dark red line) and FIXED_SN_ENERGY (yellow line) runs are actually significant. VARIABLE_SN_ENERGY peaks at around $Z/Z_\odot < -0.8$ with a tail to higher values. The entire distribution below a metallicity of around $\log Z/Z_\odot = -0.5$ is shifted to lower values for FIXED_SN_ENERGY. Because of the increased SN energy, many more metals escape the disc.

The strong effect induced by differences in the model can be seen in the metallicity distribution of stars formed. This is shown in the lower panel of Fig. 11. Most stars in VARIABLE_SN_ENERGY have $\log Z/Z_\odot < -1.0$, but the distribution exhibits a long, extended tail to higher metallicity with a second peak at supersolar values. This tail is not (or almost not) present in FIXED_SN_ENERGY. It is produced by the high-mass stars that do not inject energy but deposit large amount of metals in the gas. This highly enriched gas quickly cools and is turned into stars. When there is equal energy injection for every massive star, the injected metals are more quickly blown out and do not collapse to form these highly enriched stars. The mean (log-averaged) stellar metallicity is -1.45 for VARIABLE_SN_ENERGY. With a final stellar mass of $\sim 3.5 \times 10^7 M_\odot$, this easily matches the mass–metallicity relation within the scatter. The mean stellar metallicities are -1.80 and -1.47 for the runs FIXED_SN_ENERGY and NO_FB, respectively.
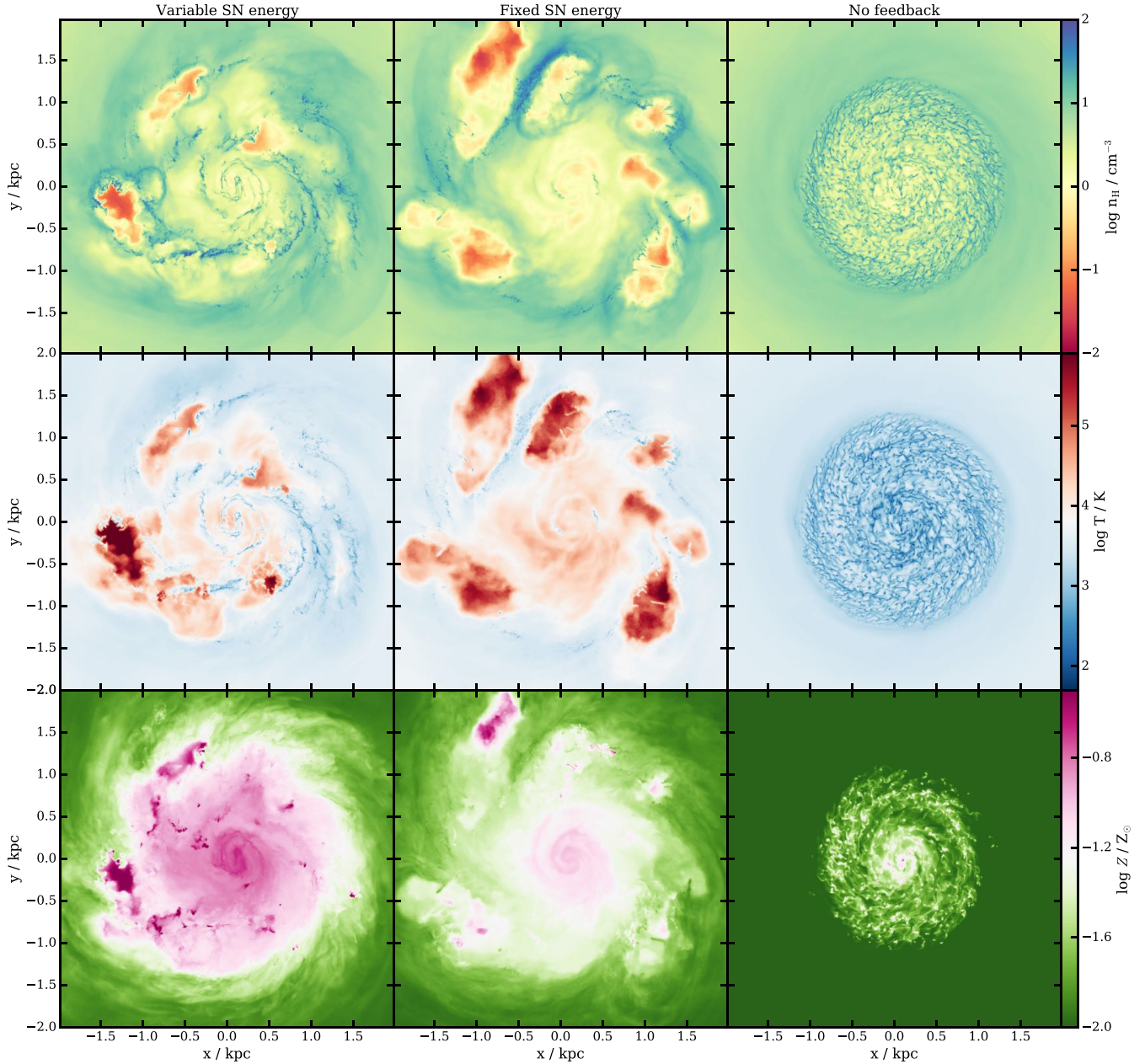
Figure 8. Face on density-weighted projections through the gas of our various isolated runs. Upper row: hydrogen number density; middle row: temperature; lower row: metallicity. As labelled above the panels, the different columns correspond to the different runs, from left to right: VARIABLE_SN_ENERGY, FIXED_SN_ENERGY, and NO_FB, respectively. The simulation time is 500 Myr.

4.5 Stellar and SN clustering

We investigate the clustering of young stars by means of the projected two-point correlation function $\omega(r)$. We use the definition presented in Landy & Szalay (1993) to calculate the autocorrelation of young stars that formed in the last 1 Myr, for which the distance r is measured in two dimensions in the plane of the disc. To increase statistics, we sum the contribution over 100 Myr, from $t = 50$ to 150 Myr where the SFR is highest. The black symbols in Fig. 12 show $\omega_{\star\star}(r)$ for young stars in VARIABLE_SN_ENERGY. There is a clear clustering signal starting at $\sim$150 pc. We fit this with a simple least-squares power law and obtain a slope of $\alpha = -1.5$, as shown in the legend. Grasha et al. (2015) calculated the power-law slope of stellar clustering for the star-forming galaxy NGC 628 and

obtain a mean slope of -0.8 with a break at 158 pc. Indeed, their youngest subsample (ages <10 Myr) exhibits a slope of -1.51. So, the clustering strength and extent of our simulated stars seem well in line with expectations from observations. This may be connected to our choice of the SF threshold (cf. Buck, Dutton & Macciò 2019).

We additionally compare the cross-correlation function $\omega_{SN\star}(r)$ of recent SN ($2 > t_{SN} > 1$ Myr) with young stars (<1 Myr) to investigate how much a SN will affect the SF in its vicinity in 1 Myr. This is presented as the blue symbols and the corresponding fit in Fig. 12. The break remains at approximately the same radius of $\sim$150 pc. However, the slope is now strongly reduced to -0.94. This is a quantitative measure of how well SN feedback is able to suppress SF. While Fig. 6 hints at a possible positive feedback effect,
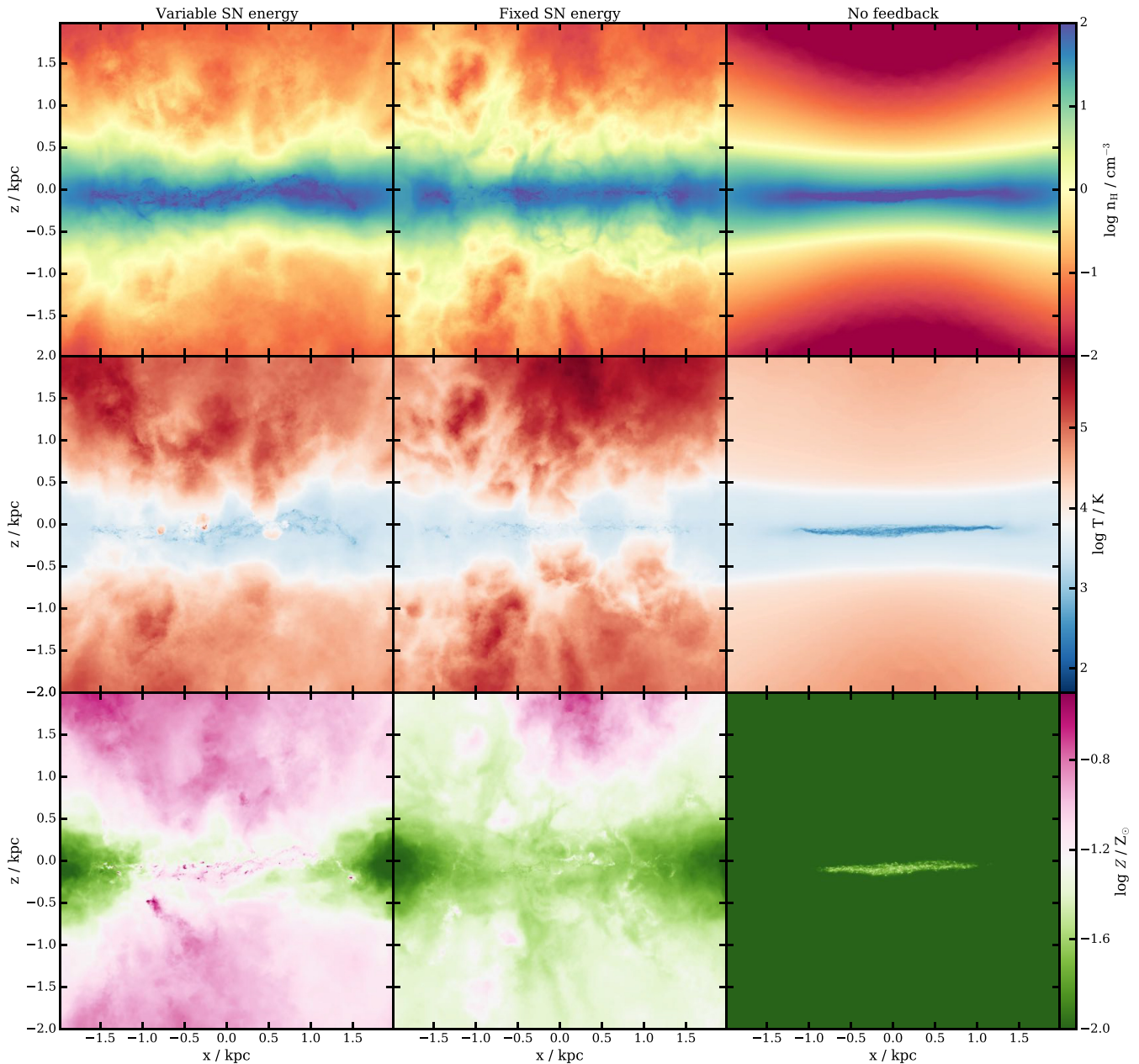
**Figure 9.** Same as Fig. 8, but edge on projections.

where SN induces new SF at the edge of their bubbles, this cannot be directly seen in this cross-correlation measurement. Nevertheless, it also does not rule out a presence of this effect entirely. While the suppressive effect of SNe is clearly dominant, some induced SF could still be present, albeit as a weaker effect.

Lastly, in Fig. 12, we also show the autocorrelation $\omega_{\star\star,\,\mathrm{NoFB}}(r)$ of young stars in NO_FB in orange. Here we see much stronger clustering at smaller radii, with a slope of -1.8 and a break at ~30 pc. A comparison of the black and orange lines tells us that SNe tend to prevent the formation of small, tight clusters. Instead, the small-scale clustering of stars is reduced somewhat and spread out to larger distances. Since the stars form in clusters, this inevitably means the SN explosions happen in a clustered manner as well. This has profound repercussions for the effectiveness of feedback (see e.g. Gatto et al. 2015; Fielding, Quataert & Martizzi 2018; Hu 2019).

As described in Section 3, the density into which a SN blast wave moves determines how well our model is able to resolve it. But more importantly, SN energy moving into a low-density region will heat a larger volume and result in reduced SF, thus making the feedback effect more pronounced.

The upper panels of Fig. 13 show the density distribution of the cells into which our dying stars inject mass, metals, and, in the case of the SN, energy. The colour coding is the same as in Fig. 4. The left-hand panels show the distribution for the AGB returns, the central panel shows the SNe and the right-hand panel shows the 'direct collapse' stars, the massive stars that die without injecting energy. The density distribution is very similar in all runs with SNe. The AGB stars are injected into $\sim10^{-4}$ cm^{-3} gas. The SNe also have a peak at 10^{-4} cm^{-3}, but displays a second smaller peak at 10^3–10^4 cm^{-3}. This broad distribution is consistent with the 'SN only' run in H17,
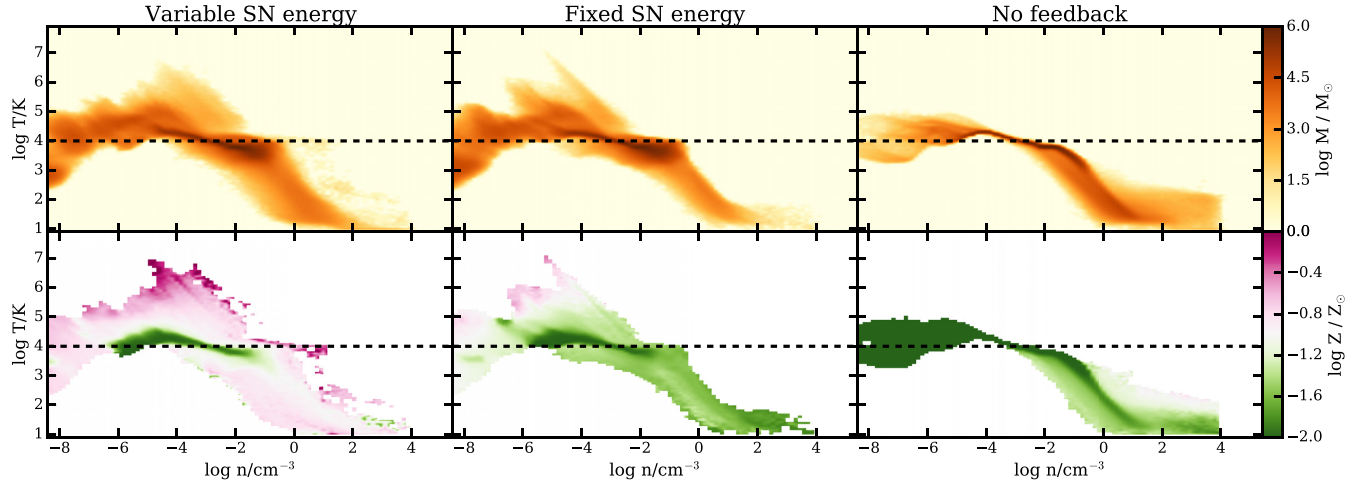
Figure 10. Mass (upper panels) and metallicity-weighted (lower panels) phase diagrams of our various isolated runs. Models with feedback exhibit a clear hot phase at lower densities (top left-hand quadrant) that models without feedback lack. Metals are injected with the SNe, so the hot phase is also metal enriched relative to the disc gas that mainly sits a 10^4 K.
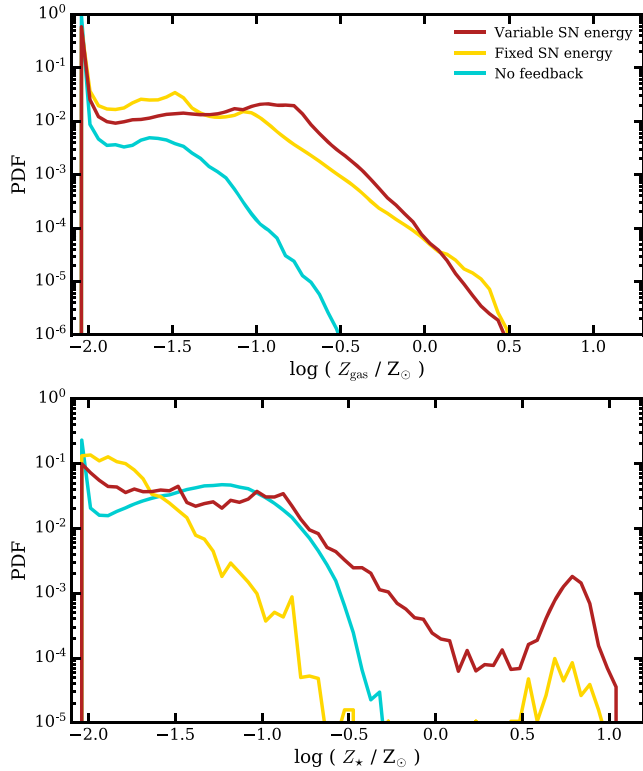
Figure 11. Metallicity distribution function of gas cells (upper panel) and stars (lower panel) in our various isolated runs. FIXED_SN_ENERGY has a lower average gas metallicity because more metals are expelled earlier. Because of this and stronger metal mixing, the stellar metallicity does not establish the same bimodal feature as exhibited by VARIABLE_SN_ENERGY.

which is, however, somewhat less bimodal. The direct collapse stars are reversed, their main peak is at high density but a small peak at low density is also present.

To help understand these distributions, we also show the mean lifetime of stars in each density bin in the lower panels. The direct collapse stars have the shortest lifetimes since they have the most massive progenitors. All runs with SNe show a clear trend that the
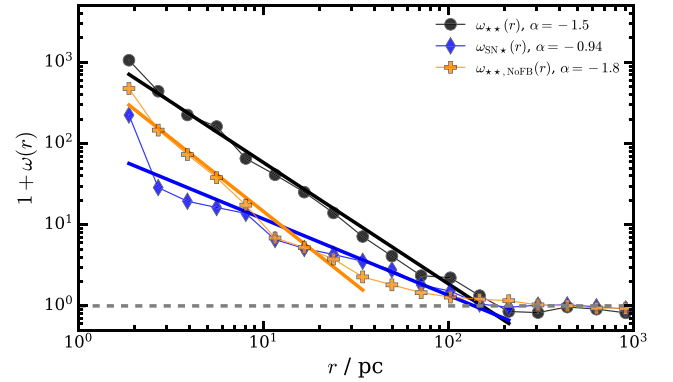
Figure 12. Two-point correlation functions for young star particles in 2D, averaged over 40 Myr between $t = 80$ and 120 Myr. Black circles represent the autocorrelation function of young stars (age <1 Myr) in the VARIABLE_SN_ENERGY model. Blue diamonds represent the cross-correlation of recent SN ($2 > t_{SN} > 1$ Myr) and young stars (age <1 Myr). The orange crosses represent the autocorrelation of young stars in NO_FB. Thick lines with different colours show power-law fits for the different cases, whose slopes α are given in the legend. The black and blue fits were calculated in the range $1 < r < 200$ pc, while the orange line was fit for the range $1 < r < 30$ pc.

shortest lived massive stars die in the highest density, while the longer lived stars inject their mass in lower density regions. This trend is the same for the SN (lower, central panel). The AGB stars have a slightly different trend, since they live long enough that the effect of the SN bubbles originating from their birth environment is not felt any longer.

So the most massive stars inject their feedback in gas that is very close to the density of SF. Once the first SN explodes, an underdense bubble is produced that has an average density of 10^{-3}–10^{-4} cm^{-3}. The longer lived stars increasingly inject their returns into this density rather than into gas that is close to the SF threshold density. The runs without SNe have a strikingly different distribution. The AGB mass returns are primarily injected into gas that has a density close to our SF threshold. This makes it apparent that the low-density injection seen in the runs with SNe is driven by SN clustering, or more accurately stellar clustering. For the runs without SNe the AGB lifetimes (blue and violet lines in the lower left-hand panel)
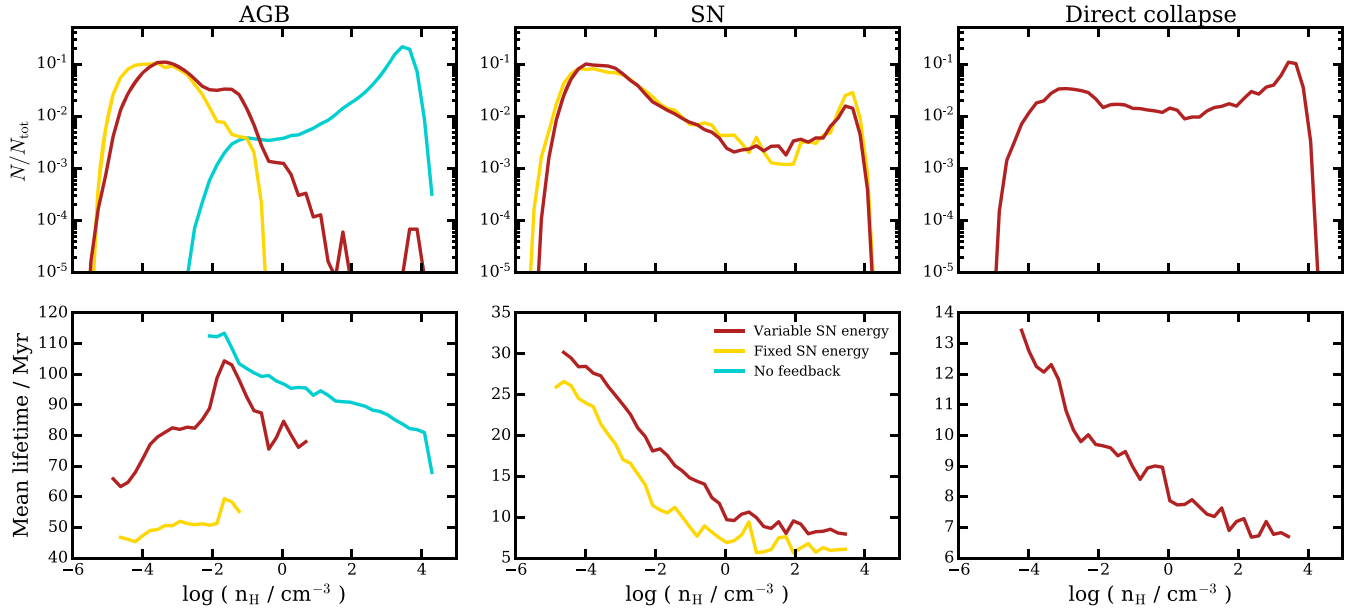
Figure 13. Probability density function (PDF) of the gas density of cells (upper panels) and the mean lifetime of stars binned by the cell density where the stars end their lives (lower panels) and inject mass and metals (and energy in the case of the SNe) in our various isolated runs, for AGB (left), SN (centre), and direct collapse stars (right) The shortest lived SNe are exploding in gas at the SF threshold. However, the majority of the SNe occur in pre-evacuated bubbles at much lower densities of $\sim 10^{-4}$ cm^{-3}.

nevertheless exhibit a trend with density. This can be attributed to the fact that their lifetimes are very long relative to the SF cycle. This allows them to wander away from their birth environment, tending towards lower density given more time.

4.6 Mass, metal, and energy loading

We now turn to an investigation of the outflows caused by our SNe. The mass loading factor attempts to quantify the amount of outflowing mass relative to the amount of SF at a given time. While it is slightly arbitrary where and how the outflowing mass is measured, we choose to measure the mass of gas in cylindrical slabs above and below the disc placed at 2 kpc distance from the plane of the disc. The radius of this cylindrical slab is set to the maximum radius of stars at that time. Its thickness is d$L = 50$ pc. We sum all mass m_i of gas within this cylinder that has a positive v_z velocity component (or negative in the case of the cylinder below the disc):

$$\dot{M}_{\rm out} = \frac{\sum m_i v_{z,i}}{{\rm d}L}. \qquad (8)$$

While this measures any local turbulence as additional mass loading, we stick to this definition for the sake of a fair comparison with other work such as H17. The metal loading, $\eta_{\rm M}$, is then computed as the outflow rate $\dot{M}_{\rm out}$ divided by the SFR. In the upper panel of Fig. 14, we show this value as a function of time in the simulation. VARIABLE_SN_ENERGY exhibits mass loading factors averaging around 1–10, which is similar to the values reported in H17 and Hu (2019). FIXED_SN_ENERGY has a higher mass loading, reaching values of 1000. This is due to the overall more energetic feedback. Runs without energetic SN have zero mass loading.

In turn, the metal loading factor η_Z attempts to quantify the amount of metals ejected from the disc relative to the metals created by the SF process. As such, it can be computed as (cf. Emerick et al. 2019)

$$\eta_Z = \frac{\dot{M}_{\rm Z,out}}{\rm SFR} \frac{M_\star}{M_Z}, \qquad (9)$$

where $M_\star$ is the stellar mass at each time and M_Z is the total metal mass created in the simulation at the corresponding time. We measure $\dot{M}_{\rm Z,out}$ in the same way as $\dot{M}_{\rm out}$, and show the evolution of this value in the central panel of Fig. 14. Metal loading factors are similar in all runs with SNe and increase throughout the simulation. The increase is in part due to the decreasing SFR. The values start at around 0.1 and increase to ~ 1. This is not entirely unexpected. Emerick et al. (2019, hereafter E19) show metal loading factors for their 10^9 M$_\odot$ isolated dwarf, also finding values of order unity. Also, Hu (2019) measure enrichment factors of 1–2, which is slightly higher than our values. Chisholm, Tremonti & Leitherer (2018) use archival the *Hubble Space Telescope* (*HST*) data to investigate the outflow properties of a small sample of galaxies and show that strongly metal-enriched outflows shape the mass–metallicity relation for dwarf galaxies. They measure metal loading factors of >100 for two dwarf galaxies with stellar masses around 10^7 M$_\odot$. However, they divide the outflow rate by the mean ISM metallicity instead of the produced metal mass, since this is not available from observations. Thus, this value is not directly comparable to the simulation definition.

The lower panel of Fig. 14 shows the energy loading, $\eta_{\rm E}$. Consistent with the previous definitions of loading factors, this is defined as the energy outflow rate divided by the energy injection rate. We obtain a value of ~ 0.1 at the beginning of the simulation, which then flattens to below 10^{-3} staying approximately constant until the end of 1 Gyr.

4.7 Phases of the ISM

As Mac Low & McCray (1988) and others have shown, the primary driver of outflows is the hot gas ($\sim 10^6$ K) within the disc that is overpressurized and blows bubbles of gas into the circumgalactic medium (CGM). The ISM is dominated in volume by hot gas in which individual cold, dense clumps sit. This is why momentum injection schemes for SN feedback are less well equipped to form a multiphase medium and reduce SF. In this section, we investigate the
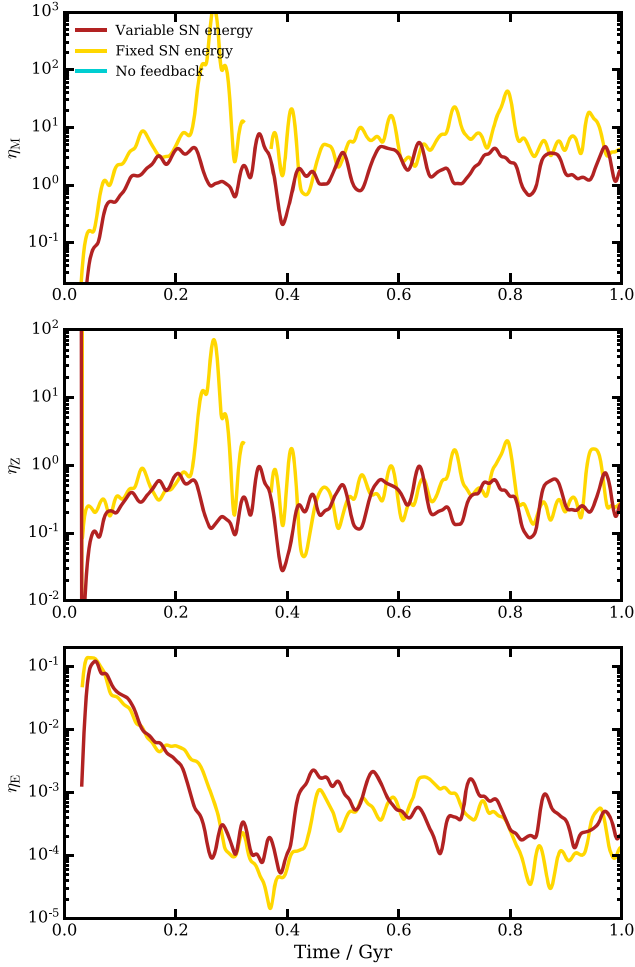
Figure 14. Mass, metal mass, and energy loading over time in our various isolated runs. Runs without SNe have zero mass loading. The VARIABLE_SN_ENERGY run shows a reduced mass loading with respect to FIXED_SN_ENERGY by a factor of 2–3.

phase components of our ISM. As above, the ISM is defined within a cylinder centred on the disc with radius equal to the maximum stellar radius and height above the mid-plane of 200 pc.

To better understand the structure of the ISM in our simulations, we split it into four phases: the hot ionized medium (HIM, $T > 10^{5.5}$ K), the warm ionized medium (WIM, $10^4 < T < 10^{5.5}$ K), the warm neutral medium (WNM, $10^2 < T < 10^4$ K), and finally the cold neutral medium (CNM, $T < 10^2$ K). Fig. 15 shows the mass and volume fractions of these four phases within the disc over time. The WNM comprises approximately 80–90 per cent of the mass at all times (after the burn-in phase) with most of the rest of the mass sitting in the CNM phase. The volume is also dominated by the WNM with most of the rest of the volume in the WIM and around 10 per cent in the HIM. If we turn to the top panel of Fig. 16, we can see the distribution of pressure within each phase. The bulk of CNM, WNM, and WIM are in pressure equilibrium. However, there is a tail of CNM at higher pressures that constitutes most of the SF gas. The HIM has overall higher pressures. This is recently shock-heated gas from SNe that is overpressurized. When this begins to cool, it forms the large tail to very high pressures of $>10^5$ K cm^{-3} in the WIM and the WNM.

Lastly, the lower panel of Fig. 16 shows the metallicity distribution within each ISM phase. The neutral media peak at just below a
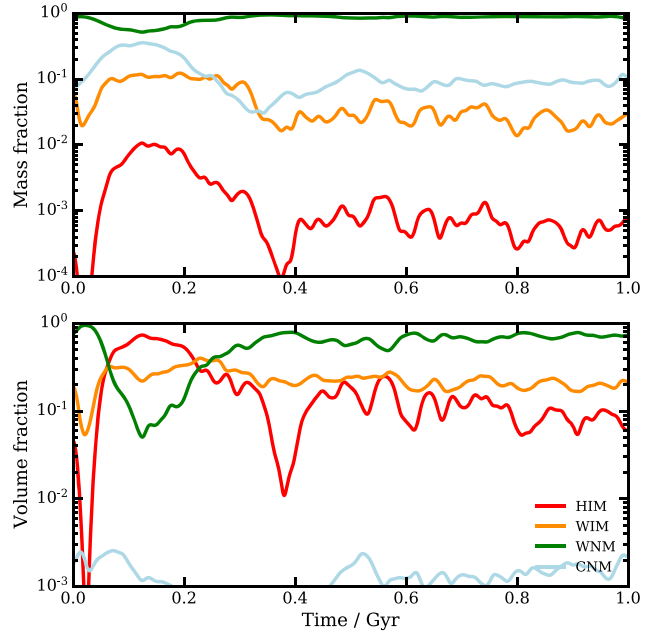
Figure 15. Fraction of gas within the disc in the phases HIM, WIM, WNM, and CNM, as a function of time for the run VARIABLE_SN_ENERGY. The upper panel shows the distribution weighted by the mass, while the lower panel applies a weighting by the volume instead. The disc is defined as a cylinder with height 200 pc above the plane, and a radius given by the maximum radius of a star at that time. While the HIM makes up less than 1 per cent of the mass, it occupies 10–20 per cent of the volume of the ISM and is responsible for driving outflows.
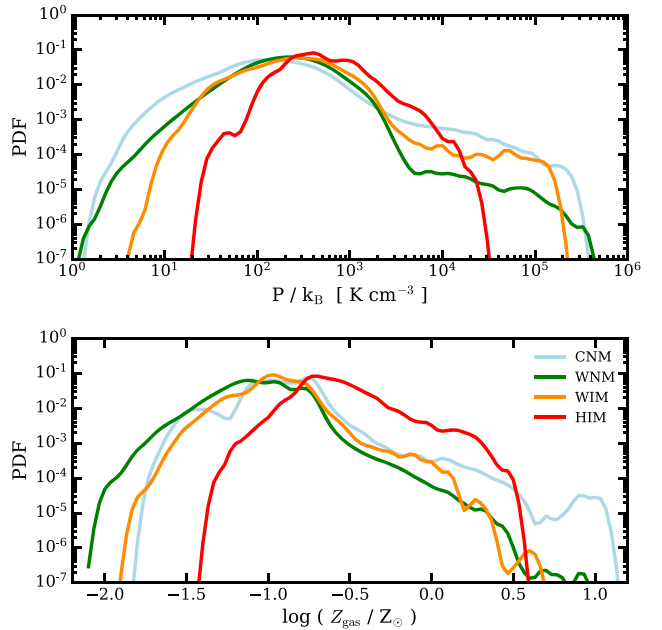
Figure 16. Pressure and metallicity probability density function (PDF) of each ISM phase within the disc after 1 Gyr for the VARIABLE_SN_ENERGY model. The CNM, WNM, and WIM are in pressure equilibrium. However, the CNM exhibits a tail to higher pressure that constitutes the majority of SF gas. The HIM is overpressurized, reflecting the hot, expanding SN bubbles.

metallicity of −1. Whereas the HIM peaks at a value of −0.6, it has a long tail to very high metallicities well above solar. This phase is the first to be enriched by the SNe, since as we know from Fig. 13, most SNe are injected in low-density material. Since the SNe are injected with energy and metals simultaneously, it is not surprising that the metallicity in the hot phase is the highest. However, from Fig. 15 we also know that the CNM carries the most mass. Indeed, despite its lower overall metallicity, the majority of metal mass is locked up in the neutral medium. The ionized media hold a mere 2–3 per cent of the metal mass. The enrichment of the neutral media is slower and can be caused either by blast waves penetrating cold clouds at their edges, or by hot enriched gas recooling into the colder phases.

5 DISCUSSION

5.1 Comparison to other simulations

While our new model is similar in nature to other simulation projects in the literature, we believe we have made some significant advancements. Here, we would like to highlight some of the differences to previous work.

As we have used the same initial conditions as Hu et al. (2016) and H17, we will compare to their results first. H17 use the SPH code GADGET-3 with the improved SPHGal formulation of SPH and set their mass resolution to $m_{gas} = 4 \, M_\odot$. A chemical network of H_2, H+, and CO allows for the formation of a multiphase ISM. The authors also include radiation from young stars that is responsible for photoheating. Cosmic rays and various chemical processes are followed to estimate the heating and cooling of the gas. This interstellar radiation field (ISRF) may initially reduce the SFR and later help maintain a steady rate.

The 'noPE-noPI-SN' model of H17 includes the most similar set of physics relative to our model. In this model, the SFH peaks at a value of around $10^{-3} \, M_\odot \, yr^{-1}$ and then flattens at around $2 \times 10^{-4} \, M_\odot \, yr^{-1}$. This is approximately an order of magnitude below our SFH. Our initial burst of SF is driven by triggered SF, which is not seen to this extent in H17. There are a variety of model choices that differ and may account for the altered SFH. Possibly the largest difference is that H17 use an SPH code while our model employs a moving mesh algorithm. This may cause the density peak of the shock within the SN shells to be more resolved with AREPO and therefore produce higher densities leading to more SF.

We choose 0.5 pc softening for the gas and 10 pc for the dark matter. H17 use 2 and 62 pc, respectively. When we test our model with the same softening values as H17, our SFR is reduced by more than a factor of 2 (see Fig. A1). Also, we set our SF threshold density to $10^3 \, cm^{-3}$, while H17 use a Jeans mass threshold where the mean density of SF is around an order of magnitude lower than ours. As such, the gas disc in our model is able to collapse to a thinner plane due to our smaller gas softening and it is given more time to collapse initially due to our higher SF density threshold. Thus, we get a higher initial burst in SF. The SN shock waves from this burst consequently trigger further SF in the adjacent clouds before the effects of negative feedback are able to set in. We do note that a further difference between the models is that the starting metallicity is $0.1 \, Z_\odot$ in H17 instead of our $0.01 \, Z_\odot$.

In general, however, our ISM structure is broadly consistent with the properties presented in H17. They report mass loading factors of 5–10, which is in the same range as ours. This is not surprising given that the hot gas fractions we find in the last 500 Myr are also consistent with their values: their mass fraction in hot gas is around 2×10^{-3},

and the volume fraction is 0.05–0.1. Similar hot gas fractions are consequently expected to drive corresponding outflows. However, H17's SNe injection density distribution peaks around $10^{-2} \, cm^{-3}$, which is two orders of magnitude higher than our finding. But since our SNe produce triggered SF, we have a higher escape fraction and thus a lower gas surface density toward the end of the simulation, which may account for the difference.

Another similar model is presented by E19, who use the ENZO code to run an isolated dwarf galaxy (halo mass of $10^9 \, M_\odot$, one order of magnitude smaller than our isolated halo) with feedback from individual stars. Their implementation includes direct star-by-star modelling, stellar winds from massive and AGB stars, and an adaptive ray tracing method to include stellar radiation. They also track non-equilibrium chemistry using the GRACKLE code. SF proceeds stochastically and each cell produces $\sim 100 \, M_\odot$ of stars stochastically drawn from the IMF. The formed stars are randomly placed within cell, which at the highest resolution level corresponds to a size of 1.8 pc. Their feedback prescription drives large outflows with mass loading factors of ~ 50 at $0.25 R_{crit, 200}$, and ~ 10 at $R_{crit, 200}$. They show that ~ 4 per cent of metals are retained in the disc, while ~ 50 per cent are ejected beyond $R_{crit, 200}$. Despite their smaller halo, these values are very similar to ours, with ~ 60 per cent of metals being blown beyond $R_{crit, 200}$ in this model. E19 also report hot phase (same as HIM in this work) mass fractions around 10^{-3} and volume fractions around 2–3 per cent. Their density distribution of SN sites peaks at $10^{-3} \, cm^{-3}$ in E19, see appendix C that is 1 dex higher than what we find. We note that the SN sites are highly dependent on the SF prescription and the SN injection mechanism. Thus, differences of this magnitude are not unexpected.

Using the Feedback In Realistic Environments (FIRE) suite, Muratov et al. (2015) investigate the outflow properties in their simulations. For their smallest galaxies 'm09' and 'm10' they report mass loading factors of 100–1000. This is significantly higher than the mass loading we measure. However, their simulations have a qualitatively different implementation of feedback, and are run at much lower resolution. An additional hindrance to a quantitative comparison is that our present simulation is based on an idealized, non-cosmological set-up. On the other hand, the stratified disc presented in Fielding et al. (2017) exhibits mass loading factors of around 0.1–1, which is somewhat below our values. The authors show that mass loading is sensitive to resolution effects and to the extent of SN clustering. Smith et al. (2019) also report much higher SN injection densities for their simulation, peaking around $10^4 \, cm^{-3}$. Since they use a thermal plus momentum injection scheme for their SNe, it is plausible that they do not produce a volume filling hot phase within the ISM to drive outflows and reduce the gas density. This may explain their much higher SN injection density distribution. Note that our SN density is based only on the cell itself, not a region of injection. This is different from, for example, Kim & Ostriker (2017) who consider the mean density in the region of the SN bubble for this quantity. However, our density is nevertheless well below the majority of their SNe that expand into 10^{-2}–$10^{-1} \, cm^{-3}$ within the stratified discs they present.

5.2 Missing physical processes

This paper discusses the first version of the LYRA model. As such, it includes only a subset of the physical processes known to be relevant for the scales we resolve. There are various models in the literature that have investigated the addition of further physics such as magnetic fields (e.g. Pakmor & Springel 2013; Girichidis et al. 2018b), cosmic rays (e.g. Simpson et al. 2016; Girichidis et al. 2018a; Chan et al.

2019), interstellar radiation (e.g. Hopkins, Quataert & Murray 2011; Agertz et al. 2013; Rosdahl et al. 2013; Roškar et al. 2014; Peters et al. 2017; Kannan et al. 2020b), or a more detailed chemistry network (e.g. Glover et al. 2010). We consider LYRA model as a new sophisticated testing ground for many such modules and forthcoming papers will investigate these. Here, we summarize our expectations on how the missing processes may affect our present conclusions.

We expect magnetic fields to have an effect on the ISM clouds, stabilizing them against gravitational collapse, and thus reducing the SFR. Also cosmic rays that provide an additional heating source will influence when and how clouds cool.

Binary stars are not included in any form at present but will affect stellar yields and stellar lifetimes. Information about binarity could be used for an effective white dwarf formation model that could in turn be used to model the Type Ia supernova (SNIa) rate. The explicit addition of SNIa will affect the iron abundance and increase the overall metallicity. We leave an investigation of these options for future work.

Radiation from young stars may arguably be the most critical ingredient missing from the present model. This can have a profound effect on the temperature distribution of the ISM (e.g. Peters et al. 2017; Emerick, Bryan & Mac Low 2018; Agertz et al. 2020; Kannan et al. 2020b) and, thus, its capability to cool efficiently. The SFR with radiation is likely to decrease by up to an order of magnitude. The ISM is expected to harbour more gas with a temperature around 10^4 K, since radiation provides a continuous heating source directly within the ISM. Additionally, the radiation from young stars is able to pre-evacuate dense regions of SF before the first SNe explode, thereby reducing the density of SN sites and increasing the feedback efficiency of the explosions.

We do not explicitly include dust formation and destruction in the gas. However, the low-temperature cooling rates were calculated assuming the 'Orion' dust model in CLOUDY. According to Popping, Somerville & Galametz (2017), for dwarf galaxies with stellar masses below 10^7 M$_\odot$ the dominant mode of dust formation is condensation in SN remnants. Including dust explicitly may decrease the gas-phase metallicities and thus possibly also the resulting stellar metallicities, since dust formation depletes the gas.

Photoelectric (PE) heating, i.e. the heating of dust by ultraviolet photons, is a feedback process that acts on the dense ISM directly, since the relevant photons mainly originate from young stars that are still embedded in their natal gas clouds. H17 have shown that PE heating in conjunction with SNe can suppress SF by an additional factor of 2–3, relative to the effect of SNe alone. The SNe are nevertheless required, since PE heating alone is unable to develop outflows and produce a multiphase ISM. This is a much weaker suppression than reported in Forbes et al. (2016), however the authors discuss the reasons for this in detail. H17 have shown that PE heating in conjunction with SNe can suppress SF by an additional factor of 2–3, relative to the effect of SNe alone.

A metallicity dependency of SN yields is not yet implemented in this model. SN yields are not well constrained, however some models such as Woosley & Weaver (1995) predict lower total metal yields for SN progenitor stars that have lower metallicity. This effect can be up to a factor of 2 in returned metal mass if some metals are present in the progenitor. Fully primordial stars are not well understood, but SN models predict even less metal return from them. This effect may be especially important for cosmological simulations that begin with gas of primordial composition. Overall, we expect that an inclusion of metallicity-dependent yields would decrease the total metal mass produced. This, in turn, could increase cooling times and reduce SF.

Furthermore, we do not include a stellar wind model that accounts for mechanical momentum injection by young stars. Such a model is expected to further decrease the ambient density of SN sites since the wind acts before the first SNe go off. This may further increase the effectiveness of SNe driving outflows. A stellar wind model coupled to LYRA will be presented in a forthcoming paper.

6 CONCLUSION

We have presented the new LYRA model for galaxy formation, which is the first of its kind to include variable SN energy. Individual stars sampled from the IMF are traced as individual collisionless particles and follow an initial mass-dependent stellar evolution pathway. The radiative cooling of gas is modelled down to 10 K and includes a prescription for molecular hydrogen. SN events are traced individually and expel thermal energy, mass, and metals according to their progenitor mass. AGB stars, as well as the more massive direct collapse stars, return mass and metals to the ISM.

We have demonstrated that at the densities where the majority of our SNe explode, we resolve the Sedov phase and reproduce the expected amount of kinetic energy based on a purely thermal injection. This makes subgrid momentum boost prescriptions to account for resolution limitations superfluous, thereby paving the way for fully realistic treatments of the multiphase ISM in cosmological simulations of galaxy formation. We validate this new model on an isolated dwarf galaxy simulated with a very high target gas mass resolution of 4 M$_\odot$. The gravitational softening for both gas and stars is 0.5 pc in these runs.

Our main results are as follows.

(i) We find that our SN feedback prescription self-consistently produces a hot phase within the ISM that drives massive outflows, reducing gas density, and suppressing SF.

(ii) Metals are efficiently ejected from the halo through these winds, reducing the overall metallicity to observed values.

(iii) The metallicity distribution is significantly affected by the energy injection scheme. The model that accounts for direct collapse stars (without energy injection) produces a tail of high-metallicity stars. This tail is otherwise not created because the expulsion of the metals by SNe is more efficient.

(iv) A model with variable SN energy yields an altered outflow behaviour with mass loading factors of 1–10, which is lower by a factor of 2–3 with respect to corresponding fixed energy model.

(v) The variable energy model expels 8 per cent of its gas beyond the virial radius, as opposed to nearly 12 per cent in the fixed energy model.

(vi) The variable energy model expels ∼40 per cent of the metals it produces beyond the virial radius, while the fixed models expel 60–70 per cent. The higher loss of metals is related to the chimneys being wider with fixed energy.

(vii) Clustered SF plays a major role in the effectiveness of feedback. Since SF clustering leads directly to SN clustering, it ultimately significantly enhances the efficiency of the SNe in heating gas and driving winds, because the majority of explosions then occur in low-density material.

(viii) Our results are well in line with previous studies in the literature, especially with regard to the ISM phase structure and outflow behaviour of the gas. Our SFR is high in comparison to previous results, which may point toward the need for the inclusion of further feedback processes such as radiation from young stars.

(ix) Stellar evolution couples directly to the feedback. This is ignored in integrated feedback prescriptions, making them insensitive to the spatially distributed energy deposition.

The obvious next goal with LYRA is to run cosmological zoom-in simulations of field dwarf galaxies at similarly high mass resolution as presented here. These calculations will be presented in a forthcoming paper. Additionally, we are developing LYRA further, adding more physics such as magnetic fields and radiation from stars. While resolving more physics introduces further complications, it is necessary to take this step to arrive at truly faithful models of the ISM, and to begin to better understand how the small-scale details of SN feedback can affect integrated galaxy properties across cosmic times. Such models also offer the prospect to inform the development of more reliable subgrid models for galaxy formation that can be used to carry out studies of the formation of full galaxy populations at much lower resolution and in very large volumes.

ACKNOWLEDGEMENTS

DATA AVAILABILITY

The data underlying this paper were accessed from the High Performance Computing resources of the Max Planck Computing and Data Facility (MPCDF, https://www.mpcdf.mpg.de). The derived data generated in this research will be shared on reasonable request to the corresponding author.

REFERENCES

Agertz O., Kravtsov A. V., Leitner S. N., Gnedin N. Y., 2013, ApJ, 770, 25
Agertz O. et al., 2020, MNRAS, 491, 1656
Asplund M., Grevesse N., Sauval A. J., Scott P., 2009, ARA&A, 47, 481
Barnes J., Hut P., 1986, Nature, 324, 446
Belokurov V. et al., 2006, ApJ, 647, L111
Buck T., Dutton A. A., Macciò A. V., 2019, MNRAS, 486, 1481
Chan T. K., Kereš D., Hopkins P. F., Quataert E., Su K. Y., Hayward C. C., Faucher-Giguère C. A., 2019, MNRAS, 488, 3716
Chevalier R. A., 1976, ApJ, 207, 872
Chisholm J., Tremonti C., Leitherer C., 2018, MNRAS, 481, 1690
Courant R., Friedrichs K., Lewy H., 1967, IBM J. Res. Development, 11, 215
Dalla Vecchia C., Schaye J., 2008, MNRAS, 387, 1431
Dekel A., Silk J., 1986, ApJ, 303, 39
Durier F., Dalla Vecchia C., 2012, MNRAS, 419, 465
El-Zant A., Shlosman I., Hoffman Y., 2001, ApJ, 560, 636
Emerick A., Bryan G. L., Mac Low M.-M., 2018, ApJ, 865, L22
Emerick A., Bryan G. L., Mac Low M.-M., 2019, MNRAS, 482, 1304 (E19)
Emerick A., Bryan G. L., Mac Low M.-M., 2020, ApJ, 890, 155
Faucher-Giguère C.-A., 2020, MNRAS, 493, 1614
Federrath C., Banerjee R., Clark P. C., Klessen R. S., 2010, ApJ, 713, 269
Ferland G. J. et al., 2017, Rev. Mex. Astron. Astrofis., 53, 385
Fielding D., Quataert E., Martizzi D., Faucher-Giguère C.-A., 2017, MNRAS, 470, L39
Fielding D., Quataert E., Martizzi D., 2018, MNRAS, 481, 3325
Forbes J. C., Krumholz M. R., Goldbaum N. J., Dekel A., 2016, Nature, 535, 523
Frings J., Macciò A., Buck T., Penzo C., Dutton A., Blank M., Obreja A., 2017, MNRAS, 472, 3378
Gatto A. et al., 2015, MNRAS, 449, 1057
Gatto A. et al., 2017, MNRAS, 466, 1903
Girichidis P. et al., 2016, MNRAS, 456, 3432
Girichidis P., Naab T., Hanasz M., Walch S., 2018a, MNRAS, 479, 3042
Girichidis P., Seifried D., Naab T., Peters T., Walch S., Wünsch R., Glover S. C. O., Klessen R. S., 2018b, MNRAS, 480, 3511
Glover S. C. O., Mac Low M.-M., 2007, ApJ, 659, 1317
Glover S. C. O., Federrath C., Mac Low M. M., Klessen R. S., 2010, MNRAS, 404, 2
Governato F. et al., 2010, Nature, 463, 203
Governato F. et al., 2015, MNRAS, 448, 792
Grasha K. et al., 2015, ApJ, 815, 93
Haid S., Walch S., Naab T., Seifried D., Mackey J., Gatto A., 2016, MNRAS, 460, 2962
Hirai Y., Fujii M. S., Saitoh T. R., 2020, preprint (arXiv:2005.12906)
Hopkins P. F., Quataert E., Murray N., 2011, MNRAS, 417, 950
Hopkins P. F. et al., 2018, MNRAS, 480, 800
Hu C.-Y., 2019, MNRAS, 483, 3363
Hu C.-Y., Naab T., Walch S., Glover S. C. O., Clark P. C., 2016, MNRAS, 458, 3528
Hu C.-Y., Naab T., Glover S. C. O., Walch S., Clark P. C., 2017, MNRAS, 471, 2151 (H17)
Kannan R., Marinacci F., Simpson C. M., Glover S. C. O., Hernquist L., 2020a, MNRAS, 491, 2088
Kannan R., Marinacci F., Vogelsberger M., Sales L. V., Torrey P., Springel V., Hernquist L., 2020b, MNRAS, 499, 5732
Karakas A. I., Lugaro M., Carlos M., Cseh B., Kamath D., García-Hernández D. A., 2018, MNRAS, 477, 421
Katz N., Weinberg D. H., Hernquist L., 1996, ApJS, 105, 19
Kim C.-G., Ostriker E. C., 2015, ApJ, 802, 99
Kim C.-G., Ostriker E. C., 2017, ApJ, 846, 133
Kirby E. N., Cohen J. G., Guhathakurta P., Cheng L., Bullock J. S., Gallazzi A., 2013, ApJ, 779, 102
Klessen R. S., 2011, in Charbonnel C., Montmerle T., eds, EAS Publ. Ser. Vol. 51, Star Formation in the Local Universe – EES2010. EDP Sciences, Les Ulis, France, p. 133
Krumholz M. R., McKee C. F., Klein R. I., 2004, ApJ, 611, 399
Lada C. J., Lada E. A., 2003, ARA&A, 41, 57
Lahén N., Naab T., Johansson P. H., Elmegreen B., Hu C.-Y., Walch S., 2019, ApJ, 879, L18
Lahén N., Naab T., Johansson P. H., Elmegreen B., Hu C.-Y., Walch S., Steinwandel U. P., Moster B. P., 2020, ApJ, 891, 2
Landy S. D., Szalay A. S., 1993, ApJ, 412, 64
Larson R. B., 1974, MNRAS, 169, 229
Macciò A. V., Frings J., Buck T., Penzo C., Dutton A. A., Blank M., Obreja A., 2017, MNRAS, 472, 2356
Mac Low M.-M., Ferrara A., 1999, ApJ, 513, 142
Mac Low M.-M., McCray R., 1988, ApJ, 324, 776
Marinacci F., Sales L. V., Vogelsberger M., Torrey P., Springel V., 2019, MNRAS, 489, 4233
Munshi F. et al., 2013, ApJ, 766, 56
Muratov A. L., Kereš D., Faucher-Giguère C.-A., Hopkins P. F., Quataert E., Murray N., 2015, MNRAS, 454, 2691
Naab T., Ostriker J. P., 2017, ARA&A, 55, 59
Navarro J. F., White S. D. M., 1993, MNRAS, 265, 271
Oñorbe J., Boylan-Kolchin M., Bullock J. S., Hopkins P. F., Kereš D., Faucher-Giguère C.-A., Quataert E., Murray N., 2015, MNRAS, 454, 2092
Ostriker J. P., McKee C. F., 1988, Rev. Modern Phys., 60, 1
Pakmor R., Springel V., 2013, MNRAS, 432, 176
Pakmor R., Springel V., Bauer A., Mocz P., Munoz D. J., Ohlmann S. T., Schaal K., Zhu C., 2016, MNRAS, 455, 1134
Peters T. et al., 2017, MNRAS, 466, 3293
Ploeckinger S., Schaye J., 2020, MNRAS, 497, 4857

Pontzen A., Governato F., 2012, MNRAS, 421, 3464

Popping G., Somerville R. S., Galametz M., 2017, MNRAS, 471, 3152

Portinari L., Chiosi C., Bressan A., 1998, A&A, 334, 505

Rahmati A., Pawlik A. H., Raičević M., Schaye J., 2013, MNRAS, 430, 2427

Read J. I., Gilmore G., 2005, MNRAS, 356, 107

Rosdahl J., Blaizot J., Aubert D., Stranex T., Teyssier R., 2013, MNRAS, 436, 2188

Roškar R., Teyssier R., Agertz O., Wetzstein M., Moore B., 2014, MNRAS, 444, 2837

Roychowdhury S., Chengalur J. N., Kaisin S. S., Karachentsev I. D., 2014, MNRAS, 445, 1392

Saito M., 1979, PASJ, 31, 193

Sawala T., Guo Q., Scannapieco C., Jenkins A., White S., 2011, MNRAS, 413, 659

Schaye J. et al., 2015, MNRAS, 446, 521

Sedov L. I., 1959, Similarity and Dimensional Methods in Mechanics. Academic Press, New York

Simon J. D., 2019, ARA&A, 57, 375

Simpson C. M., Bryan G. L., Johnston K. V., Smith B. D., Mac Low M.-M., Sharma S., Tumlinson J., 2013, MNRAS, 432, 1989

Simpson C. M., Pakmor R., Marinacci F., Pfrommer C., Springel V., Glover S. C. O., Clark P. C., Smith R. J., 2016, ApJ, 827, L29

Smith M. C., 2020, preprint (arXiv:2010.10533)

Smith M. C., Sijacki D., Shen S., 2018, MNRAS, 478, 302

Smith M. C., Sijacki D., Shen S., 2019, MNRAS, 485, 3317

Smith R. J. et al., 2020, MNRAS, 492, 1594

Springel V., 2005, MNRAS, 364, 1105

Springel V., 2010, MNRAS, 401, 791

Springel V., Hernquist L., 2003, MNRAS, 339, 289

Steinwandel U. P., Moster B. P., Naab T., Hu C.-Y., Walch S., 2020, MNRAS, 495, 1035

Stinson G., Seth A., Katz N., Wadsley J., Governato F., Quinn T., 2006, MNRAS, 373, 1074

Sukhbold T., Ertl T., Woosley S. E., Brown J. M., Janka H. T., 2016, ApJ, 821, 38

Teich Y. G. et al., 2016, ApJ, 832, 85

Trujillo-Gomez S., Klypin A., Colín P., Ceverino D., Arraki K. S., Primack J., 2015, MNRAS, 446, 1140

Vogelsberger M., Genel S., Sijacki D., Torrey P., Springel V., Hernquist L., 2013, MNRAS, 436, 3031

Vogelsberger M. et al., 2014, MNRAS, 444, 1518

Walch S., Naab T., 2015, MNRAS, 451, 2757

Walch S. et al., 2015, MNRAS, 454, 238

Walter F., Brinks E., de Blok W. J. G., Bigiel F., Kennicutt R. C., Jr, Thornley M. D., Leroy A., 2008, AJ, 136, 2563

Weinberg M. D., Katz N., 2002, ApJ, 580, 627

Weinberger R., Springel V., Pakmor R., 2020, ApJS, 248, 32

Wheeler C. et al., 2019, MNRAS, 490, 4447

White S. D. M., Rees M. J., 1978, MNRAS, 183, 341

Wiersma R. P. C., Schaye J., Smith B. D., 2009, MNRAS, 393, 99

Willman B. et al., 2005, AJ, 129, 2692

Woosley S. E., Weaver T. A., 1995, ApJS, 101, 181

Wyder T. K. et al., 2009, ApJ, 696, 1834

SUPPORTING INFORMATION

Supplementary data are available at *MNRAS* online.

Lyra_titled.mp4

Please note: Oxford University Press is not responsible for the content or functionality of any supporting materials supplied by the authors. Any queries (other than missing material) should be directed to the corresponding author for the article.

APPENDIX A: ROBUSTNESS AND RESOLUTION TESTS

We here discuss three test simulations, varying certain parameters or aspects of our model.
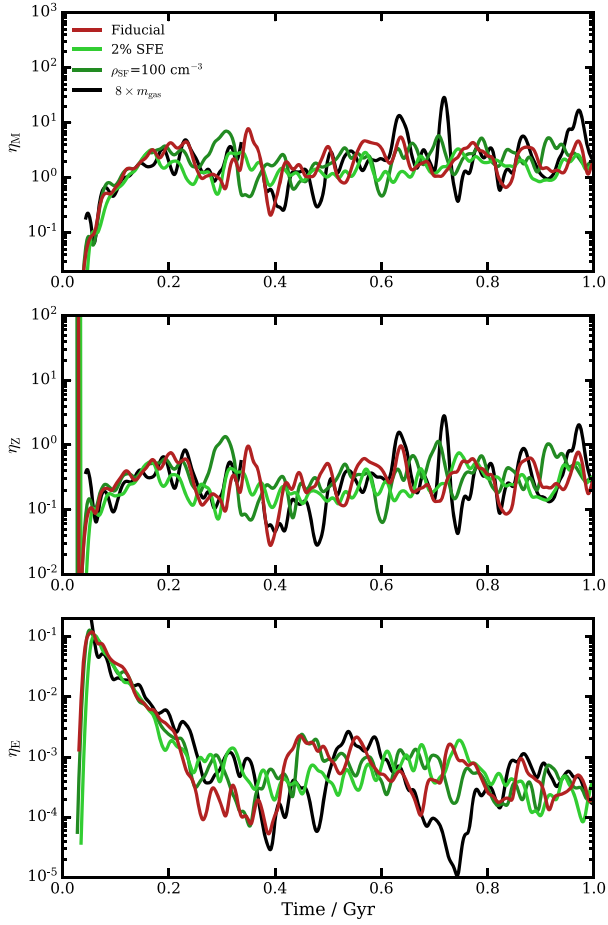
(i) $\rho_{SF} = 100 \, cm^{-3}$ means we have set the density threshold for SF to $100 \, cm^{-3}$ instead of $10^3 \, cm^{-3}$.

(ii) 2 per cent SF efficiency: we do not change the SF efficiency above $10^4 \, cm^{-3}$.

(iii) $8 \times m_{gas}$: we increase the target gas mass by a factor of 8 from 4 to 32 $M_\odot$.

Fig. A1 shows the SFH of the fiducial run and all three test runs. Neither the SF efficiency, the density threshold of SF nor a reduced mass resolution significantly alters the SFH beyond its intrinsic scatter.
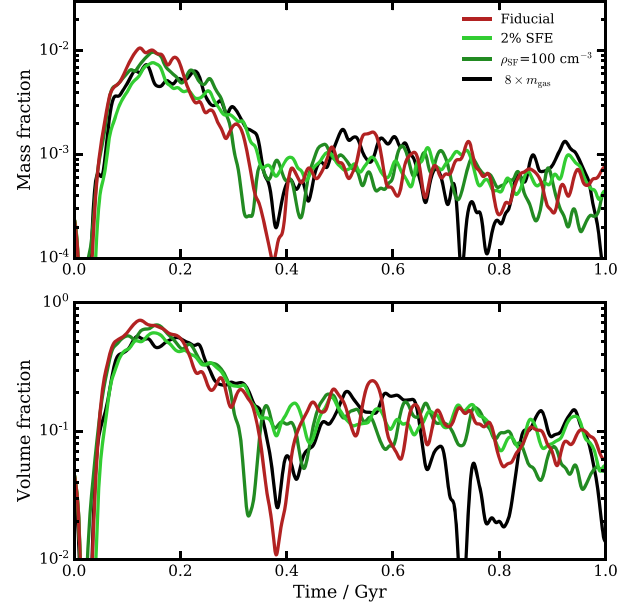
Fig. A2 shows that the mass and metal loading are insensitive to our parameter choices. Additionally, we show the mass and volume fraction of the HIM phase in Fig. A3.
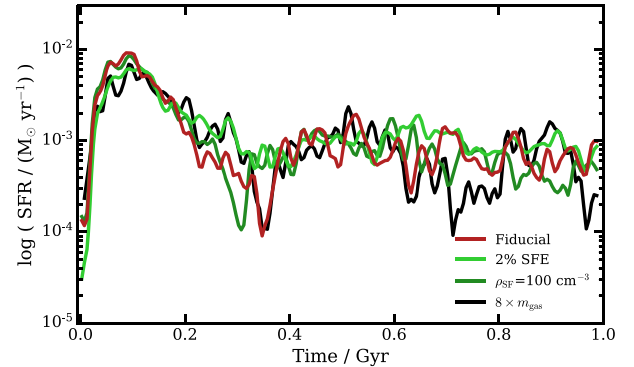
Figure A1. Star formation history (SFH) in various test runs that modify different numerical model parameters.

Figure A3. Mass and volume fractions of the HIM phase of a set of test runs that vary different numerical model parameters.

This paper has been typeset from a TEX/LATEX file prepared by the author.

Figure A2. Mass, metal mass, and energy loading of a set of test runs that vary different numerical model parameters.